Micro-nanofiber composite biomimetic conduits promote long-gap peripheral nerve regeneration in canine models

Xianhao Dong [a,1], Yueyue Yang [a,1], Zheheng Bao [b,g,1], Adam C. Midgley [a], Feiyi Li [a], Shuxin Dai [a], Zhuangzhuang Yang [a], Jin Wang [g], Lihua Liu [c], Wenlei Li [a], Yayuan Zheng [a], Siyang Liu [a], Yang Liu [c], Weijian Yu [a], Jun Liu [h,i], Meng Fan [b,***], Meifeng Zhu [a,e,**], Zhongyang Shen [d], Gu Xiaosong [f], Deling Kong [a,d,e,*]

[a] State Key Laboratory of Medicinal Chemical Biology, The Key Laboratory of Bioactive Materials, Ministry of Education, College of Life Science, Nankai University, Tianjin, China
[b] Department of Orthopaedics, Tianjin First Central Hospital, School of Medicine, Nankai University, Tianjin, China
[c] Department of Radiology, Tianjin First Central Hospital, Tianjin Medical Imaging Institute, School of Medicine, Nankai University, Tianjin, China
[d] Institute of Transplantation Medicine, NHC Key Laboratory for Critical Care Medicine, Tianjin First Central Hospital, School of Medicine, Nankai University, Tianjin, China
[e] Haihe Laboratory of Sustainable Chemical Transformations, Keyan West Road, Tianjin, 300192, China
[f] Jiangsu Key Laboratory of Neuroregeneration, Jiangsu Clinical Medicine Center of Tissue Engineering and Nerve Injury Repair, Co-innovation Center of Neuroregeneration, NMPA Key Laboratory for Research and Evaluation of Tissue Engineering Technology Products, Nantong University, Nantong, China
[g] Outpatient Department, Tianjin First Central Hospital, School of Medicine, Nankai University, Tianjin, China
[h] Clinical School/College of Orthopedics, Tianjin Medical University, Tianjin, China
[i] Department of Joint, Tianjin Hospital, Tianjin, China

A B S T R A C T

Peripheral nerve injuries may result in severe long-gap interruptions that are challenging to repair. Autografting is the gold standard surgical approach for repairing long-gap nerve injuries but can result in prominent donor-site complications. Instead, imitating the native neural microarchitecture using synthetic conduits is expected to offer an alternative strategy for improving nerve regeneration. Here, we designed nerve conduits composed of high-resolution anisotropic microfiber grid-cordes with randomly organized nanofiber sheaths to interrogate the positive effects of these biomimetic structures on peripheral nerve regeneration. Anisotropic microfiber-grids demonstrated the capacity to directionally guide Schwann cells and neurites. Nanofiber sheaths conveyed adequate elasticity and permeability, whilst exhibiting a barrier function against the infiltration of fibroblasts. We then used the composite nerve conduits bridge 30-mm long sciatic nerve defects in canine models. At 12 months post-implant, the morphometric and histological recovery, gait recovery, electrophysiological function, and degree of muscle atrophy were assessed. The newly regenerated nerve tissue that formed within the composite nerve conduits showed restored neurological functions that were superior compared to sheaths-only scaffolds and Neurolac nerve conduit controls. Our findings demonstrate the feasibility of using synthetic biophysical cues to effectively bridge long-gap peripheral nerve injuries and indicates the promising clinical application prospects of biomimetic composite nerve conduits.

1. Introduction

Peripheral nerve injury (PNI) is a common nervous system injury that is typically caused by traumatic events, surgical resection, or iatrogenic injury. PNI often leads to motor or sensory nerve dysfunction accompanied by neuropathic pain, which can seriously affect patient quality of life [1–5]. Clinically, reapproximation by end-to-end anastomosis is used to repair nerve defects with short gaps (<8 mm). Autografts are the "gold standard" for nerve defects with long gaps (>2–3 cm). However, autografting has several disadvantages that limit the scope of application, including the need for a secondary surgical procedure, limited availability of donor nerves, disruption of donor site function, size mismatch, and risk of neuroma formation [6–8]. Therefore, the development of nerve guide conduits (NGCs) offers an attractive alternative to promote the repair of long-gap nerve defects. Indeed, over 10 nerve bridging products have entered the clinical application stage [9,10].

Advances in nerve bridging products introduced scaffolds based on bottom-up (e.g., conduits, Neurolac®, NeuraGen®, NeuroTube®, etc.) and top-down (e.g., processed allografts, Avance® Nerve Graft, etc.) engineering approaches. Bottom-up constructed NGCs primarily consist of mass-produced hollow conduits of controllable size that provide axonal protection for nerve regeneration, but they have mainly been used to repair nerve defects <3 cm. Due to their lack of anisotropic guiding structures, as well as lack of pro-neuroactive substances, Schwann cell (SC) adhesion and axon elongation are unfavorable, limiting the reparative effect across defect length [11–13]. The top-down constructed NGCs typically have linear and continuous longitudinal guidance structures that closely resemble native nerves, and these have been shown to be capable of repairing nerve defects over longer distances (up to 7 cm), but the sizes and dimensions of these NGCs are limited to that of the donor nerves [11,14,15]. Comparing the above two approaches, it can be concluded that the construction of a batch-prepared NGCs that possess anisotropic guidance structures would be conducive to peripheral nerve regeneration across long-distance defects. In addition, according to feedback on the clinical application of NGCs approved by the US Food and Drug Administration (FDA), in recent years, the failure of NGCs has been attributed to lumen volume reduction, traction suture pull-out during mobility, and swelling due to material-dependent immunogenicity [16,17].

To overcome the limitations of current commercially available NGCs, an ideal nerve conduit should possess directional axonal guidance capabilities. At the same time, appropriate mechanical strength is required to avoid lumen collapse and suture pullout. Based on these necessities, we developed a composite conduit comprised of an inner anisotropic grid core structure and an outer sheath with high elasticity and porosity. Our previous studies have shown that such composite nerve conduits demonstrated convenient application with nerve regeneration capabilities in rat sciatic nerve defect models that were histologically close to the outcomes of autografting [18]. Other research groups have achieved impressive results in long-gap nerve repair in large animal models and even in humans by using conduits filled with PLGA or PLA fiber bundles [17,19], collagen fibers [20], or spider silk [21] as fibrous guides for cell attachment and migration within the conduit lumen. However, the inner diameter of such nerve conduits tends to increase, thereby distorting the arrangement of the guiding fibers and resulting in hindered axonal guidance throughout most of the lumen. Although distortion and accumulation of fibers can be mitigated by filling the lumen with many fibers, excessive use of fiber materials may trigger inflammatory responses, interfere with cell spatial arrangement and migration, and may affect the recovery of neural functionality [22–24]. To solve the above problems, we sought to precisely construct a robust guiding core with controllable fiber diameter and fiber arrangement within the three-dimensional (3D) lumen space, which helps to minimize the introduction of excess materials whilst maintaining uniform distribution of fibers throughout the lumen.

In this study, we constructed anisotropic microfiber grid cores with neural orientation guidance properties using high-resolution melt electroprinting technology. We then electrospun elastic and permeable random nanofiber outer sheaths (Schematic diagram). We compared performance of our composite nerve conduits with sheath-only conduits and the commercially available Neurolac® conduits in beagle sciatic nerve defect (3.0 cm) models. According to functional, morphological, histological, and electrophysiological analysis, nerve regeneration of the composite nerve conduits was thoroughly assessed at 1-year post-surgery. Overall, our study provides promising results that support the progress of composite nerve conduits toward translation into larger gap nerve defect repair models and pre-clinical studies.

2. Materials and methods

2.1. Material and reagents

Poly(L-lactide-co-ε-caprolactone (PLCL) pellets (70/30 L-lactide/ caprolactone copolymer, PURASORB® PLC 7015) were purchased from PURAC Biochen BV (Netherlands). Polydioxanone (PDS) pellets were purchased from Dongnan Hesheng Medical Technologies (Tianjin, China). Neurolac® nerve conduits were purchased from Polyganics Innovations BV (Netherlands). NGF and GDNF were purchased from novoprotein (Suzhou, China). Hexafluoroisopropanol (HFIP) was purchased from Aladdin (Shanghai, China). Alcohol, acetone, and xylene were obtained from Tianjin Chemical Reagent Company (Tianjin, China).

2.2. Graft fabrication

Sheath scaffold fabrication: The sheath scaffold of nerve conduits were prepared by electrospinning under the following conditions: PLCL solution (10%, w/v in HFIP), 2.0 mL/h, 21G needle, a voltage of 16 kV, a collection distance of 10.0 cm. A grounded rotating stainless-steel mandrel (4.0 mm in diameter) or plate were used as the collector. The speed of mandrel rotation was set at 200 rpm. The receiving time: 120 min for conduits and 240 min for membranes. The samples were dried in a vacuum oven at RT for 3 days to remove the residual solvent.

Core scaffold fabrication: The core scaffold of nerve conduits was prepared by using a melt electroprinting device (EFL-MDW5800, Suzhou Intelligent Manufacturing Research Institute, China) under the following conditions: The temperature of the syringe and nozzle was set to 130 °C, respectively. PDS pellets was extruded through a syringe with a 35G nozzle. Supplied air pressure was 3.80 kPa, the distance between collector and nozzle was 2 mm, and the voltage was set at 3.3 kV. Printing speed was 1800 mm/min. A total of 10 layers were printed.

Graft assembly: The intraluminal conduits were constructed by crimping and enclosing the core grid scaffold (2.8 cm in length × 2.8 cm in wide) within sheath conduits (length: 3.0 cm, internal diameter: 4.0 mm) were used for the experimental group. The sheath conduits (length: 3.0 cm, internal diameter: 4.0 mm) and Neurolac® nerve conduits (length: 3.0 cm, internal diameter: 4.0 mm) were used as control group. The entire operation was carried out in a sterile environment. Samples were sterilized by EtO gas. The basic EtO sterilization cycle was according to standard guidelines, consisting of five stages: preconditioning and humidification, gas introduction, exposure, evacuation, and air washes [25].

2.3. Graft characterization

Scanning electron microscope (SEM) measurement: The samples were mounted on aluminum stubs, sputter-coated with gold, and then examined by SEM (Quanta 200, Czech) at 15 kV.

Mechanical tests: The samples were preconditioned by incubation in PBS at 37 °C overnight and were immediately tested after being removed from the incubator. The longitudinal tensile loading and cyclic
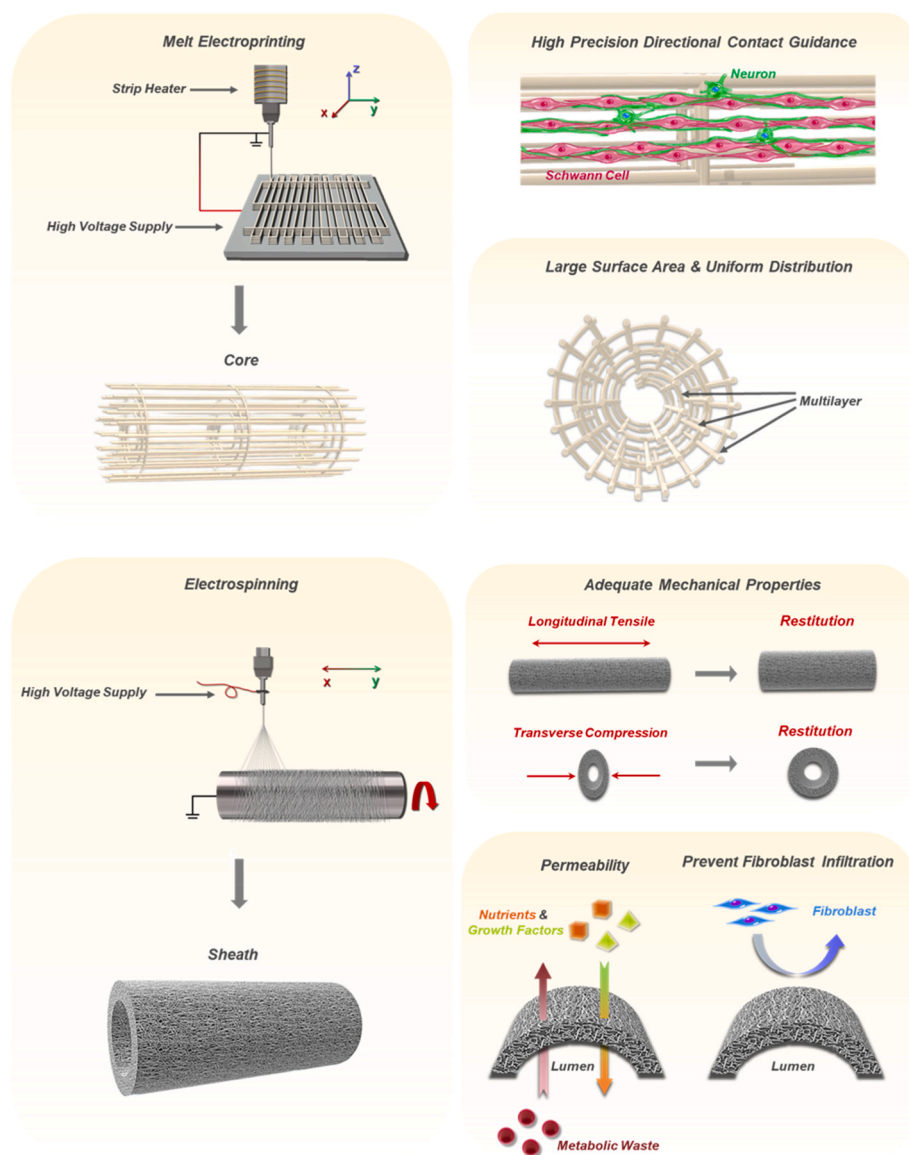
Schematic diagram. Preparation method and characteristics of composite nerve conduit. (A) The grid core scaffold was prepared by melt electroprinting. The anisotropic PDS grid had accurately controlled arrangement and diameter of fibers, supported the directional arrangement of nerve cells, and had a large surface area and uniform distribution in the lumen. (B) The nanofiber sheath scaffold was constructed using electrospinning. The randomly arranged PLCL tube with elasticity and extrusion resistance, supported the exchange of nutrients, growth factors, and metabolic waste, and could effectively block the infiltration of fibroblasts into the lumen.

compression of the conduits were carried out on a uniaxial tensile testing machine (Instron 3345, Boston, MA, USA) with 100 cycles of compression and a radial compressive stiffness at 50% strain. The end of the conduit was sutured with 6–0 suture, and the suture retention strength was recorded until the conduit knot broke (n = 5).

Molecular permeability analysis: A standard jacketed Franz Diffusion Cell with a 9 mm orifice diameter, flat ground joint, and 4.5 mL receptor volume (PermeGear, PA, USA) was prepared. The donor chamber was filled with 0.6 ml of toluidine blue with the concentration of 9 mg/mL or BSA solution with the concentration of 20 mg/mL (n = 3). The recipient chamber was filled with 4.5 mL of PBS at the temperature of 36.5 °C with 1000 rpm of magnetic stirring. Neurolac or sheath membranes were mounted between both chambers for toluidine blue or BSA diffusion. Aliquots (50 μL) of the recipient solution were periodically collected for 30 min and the concentration of each sample was calculated.

2.4. Cell culture

The rat Schwann cells RSC96, rat pheochromocytoma cell line PC12, and mouse embryonic fibroblasts NIH 3T3 were purchased from the American Type Culture Collection (ATCC). RSC96 and 3T3 cells were cultured in DMEM high glucose (GIBCO) supplemented with 10% fetal bovine serum (FBS, BI) and 100 U/mL penicillin and 100 U/mL streptomycin in a 5% CO_2 incubator at 37 °C. PC12 cells were cultured in RPMI 1640 (Thermo Fisher Scientific) supplemented with 10% FBS (BI) and 100 U/mL penicillin and 100 U/mL streptomycin in a 5% CO_2 incubator at 37 °C.

2.5. Fibroblast blocking assay

To investigate the blocking ability of nerve conduit sheath to fibroblasts, the Matrigel (10 mg/mL, Corning, USA) was first diluted with DMEM high glucose medium at a ratio of 1:1, then the diluted Matrigel was coated on the 48-well plates at 80 μL/well. The Neurolac and sheath membranes (diameter = 1.0 cm) were further placed on the Matrigel coated plates. RSC96 cells were seeded at a density of 1×10^5 cells/well (n = 4), and then were fixed with 4% paraformaldehyde (PFA) (Solarbio, China) after 2 days cultured and stained using phalloidin-AlexaFluor 633 (Invitrogen, USA) and 4′-6-diamidino-2-phenylindole (DAPI) containing mounting solution (DAPI-Fluoromount-G, Southern Biotech, UK). The above and below of the membranes were imaged using a confocal laser scanning microscope (CLSM, Leica TCS SP8, Germany).

2.6. RSC96 cells adhesion and morphology assay

To investigate RSC96 cells adhesion and morphology, the membranes (diameter = 1.0 cm) were placed in the 48-well plates and washed three times with PBS. RSC96 cells were seeded at a density of 5 $\times$ 10^3 cells/well on Neurolac, sheath, and grid core membranes, respectively (n = 5), and then were fixed with 4% paraformaldehyde (PFA) (Solarbio, China) after 5 days cultured and stained using phalloidin-AlexaFluor 633 (Invitrogen, USA), Anti-S100β (calcium binding protein S100β, Abcam, ab52642) and DAPI (Southern Biotech, England). The CLSM (Leica TCS SP8, Germany) was used for imaging.

2.7. PC12 cells adhesion and morphology assay

To investigate PC12 cells adhesion and morphology, the membranes (diameter = 1.0 cm) were placed in the 48-well plates and washed three times with PBS. PC12 cells were seeded at a density of 5 $\times$ 10^3 cells/well on Neurolac, Sheath and Core membranes, respectively (n = 5), and then were fixed with 4% PFA (Solarbio, China) after 5 days cultured and stained using phalloidin-AlexaFluor 633 (Invitrogen, USA), Anti-β-III tubulin (Tuj-1, Abcam, ab78078) and DAPI (Southern Biotech, UK). The CLSM (Leica TCS SP8, Germany) was used for imaging.

2.8. RSC96-PC12 cells co-culture assay

The experiment was carried out by modifying previously reported methods [26]. Briefly, the membranes (diameter = 1.0 cm) were placed in the 48-well plates and washed three times with PBS. RSC96 cells were seeded at a density of 2.5 $\times$ 10^3 cells/well on Neurolac, Sheath, and Core membranes, respectively (n = 5). After 3 days culturing, 2.5 $\times$ 10^3 PC12 cells were seeded on the membranes. 50 μg/ml NGF and 50 ng/ml GDNF were added into the medium at day 4. This medium (contained NGF and GDNF) was refreshed every other day and the culture maintained for a total of 10 days. The samples were fixed with 4% PFA (Solarbio, China) and stained phalloidin-AlexaFluor 633 (Invitrogen, USA), Anti-S100 beta (Abcam, ab52642), Anti-β-III tubulin (Abcam, ab78078) and DAPI. The CLSM (Leica TCS SP8, Germany) was used for imaging.

2.9. Animal surgery and grouping situation

Nine adult male beagle dogs (9.5–10.5 kg, 8–12 months) were obtained from the Marshall Bioresources Beijing (China). All animal studies were performed according to the guidelines set by the Tianjin Committee of Use and Care of Laboratory Animals, and the overall project protocols were approved by the Animal Ethics Committee of Nankai University. The dogs were randomly divided into three groups: (i) three in the Neurolac® nerve conduit group; (ii) three in the Sheath nerve conduit group; (iii) three in the Sheath & Core nerve conduit group. Anesthesia was induced by intramuscular injection of xylazine (1.5 mg/kg). After endotracheal intubation, dogs were maintained under general anesthesia by inhalation of isoflurane (1–4%). The outside of the left thigh was shaved, then a skin incision was made along the femoral axis, the muscles outside the thigh were separated free, and a 50-mm long segment of sciatic nerve was exposed. Then a 26-mm long segment of sciatic nerve was then resected, leaving a 30-mm long defect following retraction of the nerve ends. The nerve defect was bridged by nerve conduit with both the proximal and distal nerve stumps anastomosed to the graft at each junction using a 6-0 Surgipro™ suture (COVIDIEN, USA). The muscles and skin were sutured with a 3-0 MER-SILK® suture (Johnson & Johnson Medical, USA) to close the surgical incision. Experimental end points were set at 1 year.

2.10. MRI and 3D reconstruction of nerves and muscles

MR Imaging: The canines were examined by MRI 1 year after surgery to observe the morphology of the peripheral nerve lesion site and the gastrocnemius muscle. MRI examination was performed on a 3.0T MRI scanner (Prisma, Siemens, Germany) with a 16-channel phased-array body coil. After anesthesia, canines were placed in the prone position. The imaging protocol included coronal Dixon T2WI (TR 7230 ms, TE 59 ms, slice thickness 3 mm, FOV 350 mm $\times$ 350 mm, matrix 320 $\times$ 224); coronal 3D dual echo steady state (DESS) (TR 16 ms, TE 5 ms, slice thickness 0.6 mm, FOV 170 mm $\times$ 170 mm, matrix 256 $\times$ 251, Flip angle 25, acquisition times 1); coronal DWI (TR 10520 ms, TE 53 ms, slice thickness 3 mm, FOV 380 mm $\times$ 380 mm, matrix 192 $\times$ 192, acquisition times 2), b-values were 0, 700 s/mm^2, and ADC-MAP map was automatically generated.

Imaging Analysis: All the images were explored from the picture archiving and communication system (PACS). Imaging analysis and post-processing were obtained using a software package (Mimics medical, 21.0, Belgium). Referring to T1WI, T2WI, and DWI images, the regions of interest (ROIs) were manually drawn along the gastrocnemius muscle and sciatic nerve border on all slices of ADC maps to generate a 3D-ROI by one radiologist with six years of orthopedic diagnosis experience without clinical information and verified by a senior radiologist with eight years diagnostic experience. Furthermore, another radiologist with five years of orthopedic diagnosis experience repeated this procedure alone without clinical information.

2.11. Walking track assessment

To characterize the functional recovery after 1-year post-surgery, canines were free to walk in the walkway (2 m in wide $\times$ 20 m in length) for at least 20 min. The movement of canines were video recorded using a high-speed videotaping device (Go Pro HERO 9, USA). The video data was then analyzed frame-by-frame to record the range of motion of the hip joint, knee joint, hock joint and metatarsophalangeal joint of the canine. Reconstruction of the left hindlimb joint motion within a full stride period was performed according to these data, and further normalized for the range of motion of the hock joint and the metatarsophalangeal joint. The locomotion scoring of the hind limb's movement disorder was used to further assess the functional recovery outcomes of peripheral nerve regeneration.

Score 3: Severe paralysis of the left hind limb occurred immediately after a transection of the left sciatic nerve.

Score 2: The hock joint of the left hindlimb were slightly over flexed, and the animals were able to partially lock the knee and hock joints during moving, with occasional claudication or inconsistent stride length, and were accompanied by an upturning of plantar.

Score 1: The animals were able to perform coordinated movements and regular stride intervals close to the pre-surgical state during moving, and the plantar positioning on the ground normally.

2.12. Electrophysiology assessment

To characterize the electrophysiological properties after 1-year post-surgery, Canines were anesthetized and placed in a lateral position. Compound muscle action potentials (CMAPs) and motor nerve conduction velocity (MNCV) of the sciatic nerve were measured using a neurophysiological parameter tester (NeuroCare-T, NCC MEDICAL, Shanghai, China). The recording electrode patch was attached to the gastrocnemius muscle belly, the reference electrode patch was attached to the skin surface of the lower tibia, and the stimulating electrode was successively applied to the sciatic nerve trunk at the proximal and distal ends of the graft, and the amplitude and latency of the CMAPs were recorded. Accurately measure the distance between two electrical stimulation points and calculate the MNCV. The same procedure was performed on the unaffected sciatic nerve.

2.13. Morphological and histological analysis

At 1-year post-surgery, all nerve conduits were retrieved for cutting

into sections. Sample segmentation and corresponding histological characterization were shown in Fig. 7A. For histochemical staining, the conduits were fixed in buffered 4% paraformaldehyde for 72 h, then dehydrated in a graded ethanol series, cleared in xylene, embedded in paraffin (Leica, Germany) and cut into 5-μm thick sections. The sections were stained with Hematoxylin and Eosin (H&E, Solarbio, China), Masson trichrome (Solarbio, China), Toluidine Blue (Solarbio, China), Luxol Fast Blue (Solarbio, China). Images were observed under an upright microscope (Leica, DM3000, Germany). For transmission electron microscopy (TEM), the conduits were fixed in a solution of 2.5 wt% glutaraldehyde (Solarbio, China) for 72 h and then transverse ultrathin (thickness: 50.0 nm) sections were cut on a microtome (Leica, EM UC6,

Germany), placed on 0.5% formvar coated meshes and stained with uranyl acetate and lead citrate. Images were observed under the TEM (HITACHI, HT7700 Exalens, Japan), using an accelerating voltage of 100 kV. The evaluation of the g-ratio (defined as the inner axon diameter divided by the outer diameter of the myelinated sheath) was carried out by photographing randomly selected fields of each TEM image at 1500 × magnification, and at least 100 myelinated axons were measured for each group.

2.14. Wet weight and histological assessment of gastrocnemius muscle

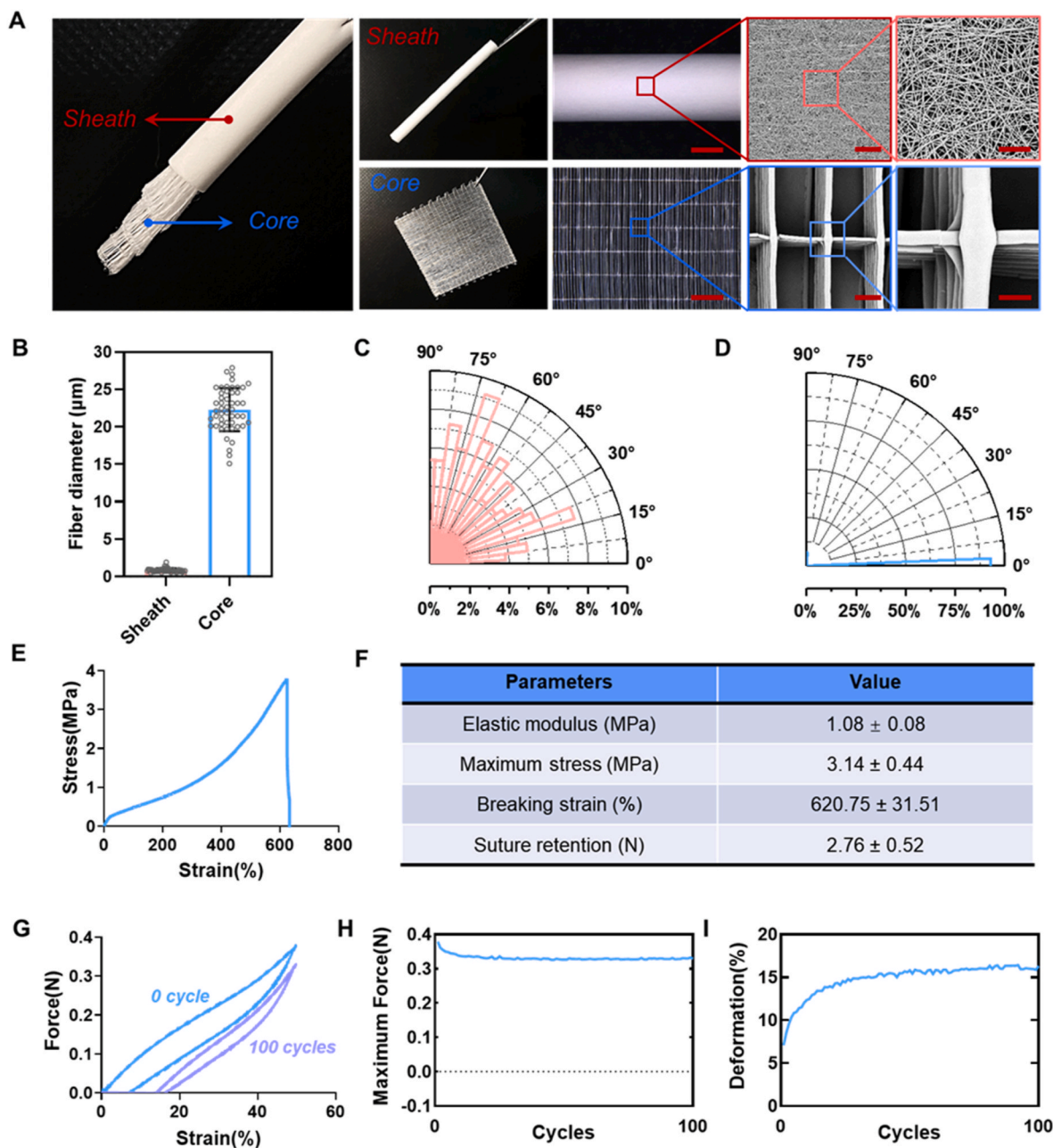The gastrocnemius muscles were harvested from both the

Fig. 1. Composite nerve conduit characterization. (A) Macroscopic and microscopic morphology of the external sheath and inner grid core of nerve conduit. **(B)** Fiber diameter of the Sheath scaffold and Core scaffold. **(C)** Nightingale rose plots of fiber orientation angle of the Sheath scaffold. **(D)** Nightingale rose plots of fiber orientation angle of the Core scaffold. **(E)** Tensile stress-strain curve of the Sheath scaffold. **(F)** Table of mechanical parameters of the Sheath scaffold. **(G)** The stress-strain curve for compression of Sheath scaffold after 100 compression cycles. **(H)** The maximum force changes of Sheath scaffold after 100 compression cycles. **(I)** The diameter deformation changes of sheath scaffolds after 100 compression cycles. Scale bars: A, the third column, 2 mm; the fourth column, 100 μm; the fifth column, 30 μm. $n = 5$ for mechanical tests.

experimental and the control sides for weighing. The muscle wet weight ratio (%) was calculated as: the muscle wet weight of the experimental limb/the weight of the contralateral control limb × 100%. After that, several pieces of the excised gastrocnemius muscle were cut from the mid-belly and fixed in buffered 4% paraformaldehyde for 72 h, then dehydrated in a graded ethanol series, cleared in xylene, embedded in paraffin (Leica, Germany) and cut into 7-μm thick sections. Pathological changes in gastrocnemius muscle were examined using H&E (Solarbio, China) staining and Masson trichrome (Solarbio, China) staining. Images were observed under an upright microscope (Leica, DM3000, Germany).

2.15. Statistical analysis

All quantitative results were obtained from at least three independent experiments for analysis. Data were expressed as the mean ± standard error of the mean (SEM). GraphPad Prism Software Version 9.0 (San Diego, CA, USA) was used for statistical analysis. Single comparisons were carried out using an unpaired student's t-test. Multiple comparisons were carried out using one-way analysis of variance (ANOVA) and Tukey's post-hoc test. The minimum significance level was set at $* p < 0.05$, $**p < 0.01$, $***p < 0.001$, and $****p < 0.0001$.

3. Results

3.1. Nerve conduits preparation and characterization

The nerve conduits in this study consisted of two parts: a random nanofiber sheath scaffold and an oriented microfiber grid core scaffold (Fig. 1A). The sheath scaffolds were prepared by electrospinning with PLCL material, which mimicked the structure of the natural epineurium ECM and facilitated suturing to the epineurium of the native nerve stump. SEM examination and measurements confirmed that the fiber diameter of the sheath scaffold was 0.83 ± 0.25 μm (Fig. 1B) with inter-fiber pore size of 4.72 ± 0.53 μm (Supplementary Fig. 1A). The inner diameter of the sheath scaffold was 3.98 mm ± 0.04 mm, and the wall thickness was 395.6 ± 12.3 μm. Nightingale Rose plots representing the broad angle distribution of random nanofibers are shown in Fig. 1C. We next tested the mechanical properties of the sheath. In the tensile tests, the representative stress-strain curve of the sheath scaffold was recorded and is shown in Fig. 1E. Results indicated an elastic modulus of 1.08 ± 0.08 MPa, a maximum stress of 3.14 ± 0.44 MPa, and a maximum strain of $620.75 \pm 31.51\%$.

To mimic changes in joint motion aggravating sutured conduits until break, we carried out the suture retention testing. The results showed that the pull-out strength of the sheath scaffold was 2.76 ± 0.52 N (Fig. 1F). In the compression cycle test, the representative stress-strain curves of the sheath scaffold after 0 and 100 compression cycles are shown in Fig. 1G. We performed a mechanical test on 50% deformed sheath scaffold (Fig. 1H) and tested the diameter deformation of the after the 100th compression cycle (Fig. 1I). Compared with the initial state, the maximum stress was reduced by $12.84 \pm 4.45\%$, and the diameter was reduced by $16.13 \pm 0.76\%$. The sheath scaffold could be easily restored to its original shape after being pressed, stretched, folded, and twisted (Supplementary Video 1). The grid core scaffolds were prepared with PDS material combined with electroprinting process, which simulated the orientation structure of nerve fibers, and served as the matrix for the directional adhesion and migration of nerve cells. SEM pictures showed that the fiber layers were stacked steadily and repeatedly as designed. The fiber diameter of the grid core scaffold was 22.29 ± 2.87 μm (Fig. 1B) and a spacing of 1500.20 ± 23.93 μm in the Y axis direction and a spacing of 158.98 ± 17.87 μm in the X axis direction were fabricated (Supplementary Fig. 1B). Nightingale Rose plot showed that the microfibers of the grid core scaffold were vertically parallel (Fig. 1D).

Supplementary video related to this article can be found at https://

3.2. Permeability and fibroblast cell barrier capacity of nerve conduits

To characterize the permeability of the Neurolac nerve conduit versus the sheath scaffold, we performed drug diffusion experiments using Franz diffusion cells (Fig. 2A). Here, we selected toluidine blue (TB, molecular weight 373.97 Da) as a representative low-molecular-weight drug and BSA (molecular weight 66.43 kDa) as a representative high-molecular-weight drug. Drug concentrations in the donor and recipient chambers were measured at different time points, TB (Fig. 2B) and BSA (Fig. 2C) diffusion curves for the Neurolac nerve conduit and TB (Fig. 2D) and BSA (Fig. 2E) diffusion curves for the Sheath scaffold were plotted, respectively. Neurolac nerve conduit was virtually impermeable to both low- and high- molecular weight drugs, which was closely related to its non-porous dense structure (Supplementary Fig. 2). However, the Sheath scaffold could achieve more than 50% TB diffusion with BSA in 5 min, and basically completed the dynamic balance of the two drugs in the donor chamber and recipient chamber at 30 min. To characterize the ability of Neurolac neuro-ducts and sheath scaffolds to block fibroblasts, we utilized Matrigel chemotaxis to investigate the number of fibroblasts crossing the membrane scaffold from above to below (Fig. 2F). The results showed that almost all fibroblasts were trapped on the upper surface of the Neurolac nerve conduit, whereas very few fibroblasts were able to cross the sheath scaffold (Fig. 2G), but there was no significant difference in the blocking rate between the two groups (Fig. 2H).

3.3. Guidance from different scaffolds for Schwann cells arrangement

To observe the arrangement and spreading of RSC96 cells on different scaffolds, the RSC96 cells were cultured for 5 days and subjected to S100β and F-actin immunofluorescence staining and CLSM imaging. The images showed that RSC96 cells clustered on the Neurolac and Sheath scaffolds, with round shape, short pseudopodia, and irregular distribution. On the grid core scaffolds, RSC96 cells were mostly arranged side by side on a single microfiber. The cells showed an elongated morphology with bipolar distribution of pseudopodia and extended along the fiber direction, forming a structure similar to the "Bungner's bands" (Fig. 3A). This is the basic structure of myelin and is known to play an important role in peripheral nerve regeneration. In addition, we counted the angle of RSC96 cell arrangement, and the results showed that Schwann cells dispersed in all directions on both Neurolac scaffolds and sheath scaffolds (Fig. 3B and C). Schwann cells were oriented on the Core scaffolds, and the cell angles were mainly distributed within 0–10° (Fig. 3D). At the same time, the length of Schwann cell pseudopodia on the grid core scaffolds was significantly higher than that of the other two groups (Fig. 3E), and the shape index was significantly lower than that of the other two groups, which further reflected the elongated morphology of the cells (Fig. 3F). The Schwann cell spreading area of Core scaffold was significantly lower than that of the other two groups, and the sheath group was also significantly lower than that of Neurolac group (Supplementary Fig. 3). The above data indicated that the grid core scaffolds had a significant directional guidance effect on Schwann cells.

3.4. Guidance from different scaffolds for neurite outgrowth

To observe the arrangement and spreading of PC12 cells on different scaffolds, PC12 cells were cultured for 5 days and subjected to β–III–tubulin and F-actin immunofluorescence staining and CLSM imaging. Significant expression of β–III–tubulin and neurite extension could be observed, indicating that PC12 cells were well differentiated on all scaffolds. The PC12 cells showed scattered distribution on both Neurolac and sheath scaffolds, accompanied by short extension of most neurites. On the grid core scaffold, PC12 cells are mostly concentrated
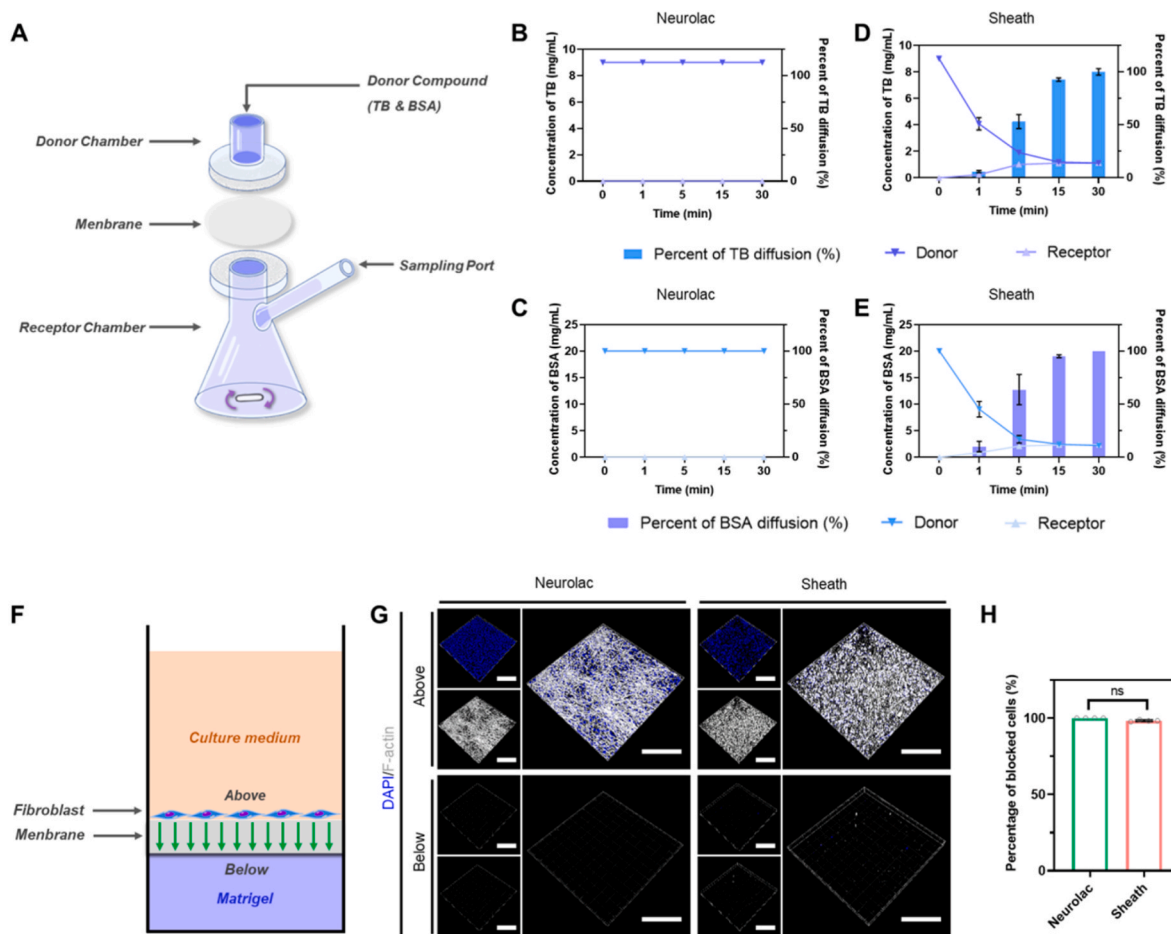
Fig. 2. Characterization of permeability and cell barrier ability of the nerve conduit. (A) Schematic diagram of drug diffusion using Franz diffusion cell. **(B)** TB diffusion curve of Neurolac nerve conduits. **(C)** BSA diffusion curve of Neurolac nerve conduit. **(D)** TB diffusion curve of the Sheath scaffold. **(E)** BSA diffusion profile of the sheath scaffold. **(F)** Schematic diagram of scaffold blocking fibroblast migration. **(G)** Representative images of cell morphology on the upper surface (first row) versus the lower surface (second row) of the scaffolds after fibroblasts were cultured on Neurolac and sheath scaffold. F-actin was stained grayish white and cell nuclei was stained blue. **(H)** The percentage of blocked fibroblast by different scaffolds. Scale bars: 200 μm. $n = 3$ for molecular permeability analysis; $n = 4$ for fibroblast blocking assay.

on individual fiber, with multiple neurite branches entangled each other and extended along the fiber direction (Fig. 4A). We quantitatively assessed the angle of neurite arrangement, with neurites scattered irregularly in all directions on both Neurolac and Sheath scaffolds (Fig. 4B and C), whereas neurites on the Core scaffolds exhibited a high degree of directional consistency (Fig. 4D). The neurite length on the Core scaffold was significantly higher than that in the other two groups, and the neurite length of Sheath scaffold was also significantly higher than that of Neurolac group (Fig. 4E). Similar to Schwann cells, the cell shape index of PC12 on the grid core scaffold was significantly lower than that of the other two groups (Fig. 4F), The PC12 cell spreading area of grid core scaffold was also significantly lower than that of the other two groups (Supplementary Fig. 4), and the above data all indicated that the grid core scaffolds had a significant directional guidance effect on neurites.

3.5. RSC96-PC12 cell co-culture on different scaffolds

To generate the RSC96-PC12 cell co-culture system, we referred to the study by Malheiro et al. [26], the culture protocol was shown in Fig. 5A. In brief, RSC96 cells were first seeded on different scaffolds and cultured for 3 days, followed by PC12 cells seeded on them and cultured for another 7 days, and NGF and GDNF were added to the culture medium during the culture period to promote differentiation and maturation of the co-culture system. Subsequently, immunofluorescence

staining for S100β, β–III–tubulin and F-actin with CLSM imaging was performed on the co-culture system. As shown in Fig. 5B, both RSC96 and PC12 cells exhibited good cell spreading and significant expression of S100β and β–III–tubulin on all three scaffolds. Interestingly, under the premise of uniform seeding of the two cells, PC12 cells in the co-culture system showed the characteristics of clumping growth on Neurolac and sheath scaffolds, with small proportion of neurites extended, which was significantly different from the state of scattered growth of PC12 cells in the culture alone. RSC96 cells in the co-culture system were radially distributed around PC12 cell spheres on Neurolac and sheath scaffolds, and some of the cells showed bi- or multi-polarized pseudopodia morphologically. The cell distribution and morphology of RSC96-PC12 co-culture system on Neurolac and sheath scaffolds closely resembled those of DRG cell spheres cultured in vitro [18,27]. On the grid core scaffolds, the cells of RSC96-PC12 co-culture system showed a state of accumulation along the single microfiber, and neurites contacted Schwann cell pseudopodia and extended along the fiber direction. We further assessed the angle of Schwann cells and neurites arrangement on different substrates under co-culture system. RSC96-PC12 cells presented a dispersed arrangement on Neurolac scaffolds and sheath scaffolds (Fig. 5C and D), and presented a parallel arrangement with fibers on grid core scaffolds (Fig. 5E). When RSC96-PC12 cells were co-cultured on three kinds of scaffolds, the pseudopodia length of Schwann cells and the neurite length were higher than that of the RSC96 cells or PC12 cells cultured individually. Quantitative statistics of
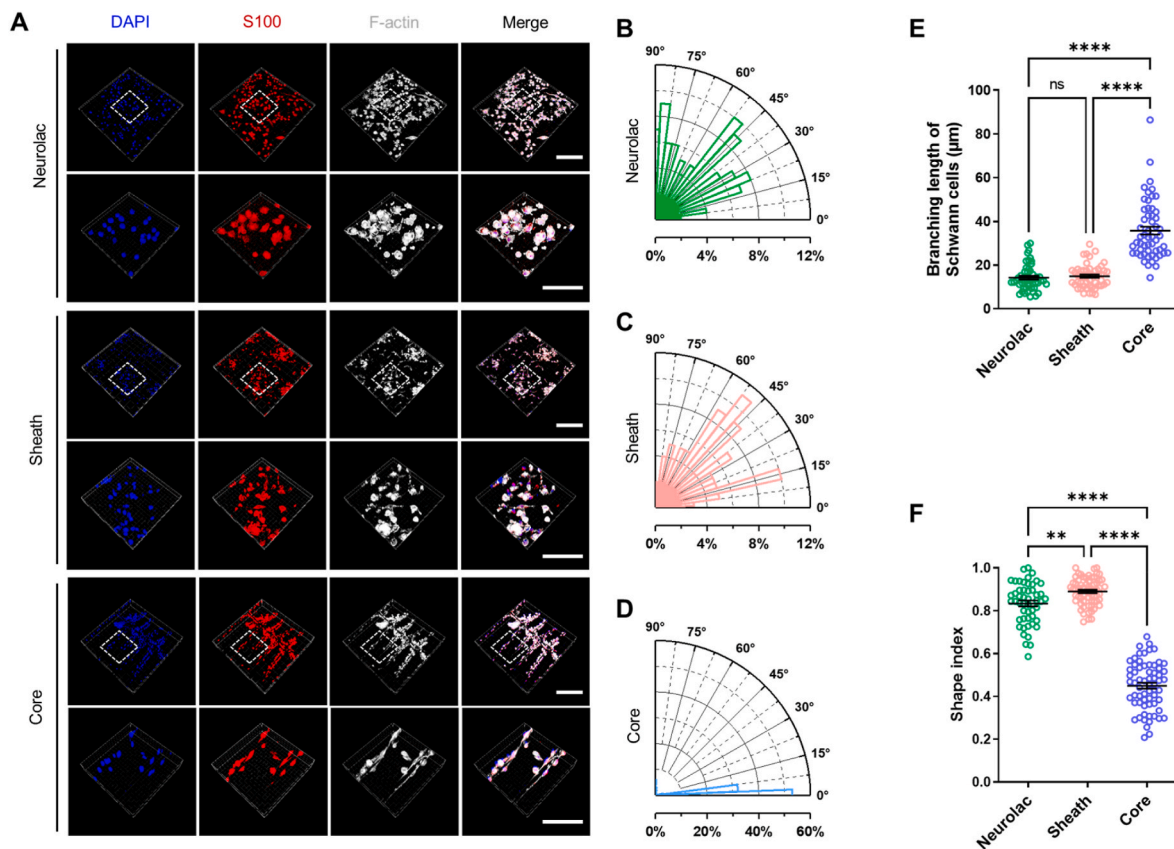
Fig. 3. Schwann cell behavior on different scaffolds. (A) Representative images of Schwann cells arranged and spread on the Neurolac scaffolds, Sheath scaffolds, and Core scaffolds, respectively. The second row of images in each group represent high-magnification images of the white box area. S100β was stained in red, F-actin was stained grayish white, and cell nuclei was stained blue. **(B, C, D)** Nightingale rose plots of Schwann cell orientation angle of the Neurolac scaffolds, Sheath scaffolds, and Core scaffolds, respectively. **(E)** The branching length of Schwann cells on different scaffolds. **(F)** The shape index of Schwann cell nucleus. Scale bars: the first row of every group, 200 μm; the second row of every group, 100 μm. $n = 5$ for all groups.

Schwann cell pseudopodia length showed that cells on the grid core scaffold had significantly higher pseudopodia length than the other two groups, while Neurolac group had no significant difference from sheath group (Fig. 5F). Quantitative statistics of neurite length showed that the neurite length on the grid core scaffold was significantly higher than that in the other two groups, and the neurite length was also significantly higher in the Sheath group than in the Neurolac Group (Fig. 5G). Further, we counted the co-localization between PC12 neurites and SCs, and the grid core scaffolds significantly enhanced the proportion of SCs adhering to neurites compared with the other two groups (Fig. 5H).

3.6. Implantation process of nerve conduits and the morphology of regenerated nerve

We next sought to verify the efficacy of nerve conduits in repairing peripheral nerve defects with large gaps (>2–3 cm). We implanted three kinds of nerve conduits (Neurolac, sheath, sheath & grid core) in a 3 cm sciatic nerve defect model in beagle dogs, and the implantation process and detection method were shown in Fig. 6A. The surgical procedure is illustrated in detail in Fig. 6B. After sciatic nerve exposure, approximately 5 cm in length of the sciatic nerve was isolated. After partial sciatic nerve removal, it was naturally retracted a 3 cm gap, and the nerve conduit was sutured using an end-to-end anastomosis. The Neurolac nerve conduits appeared transparent, and its dense structure resulted in the formation of water mist in the lumen. The sheath and sheath & grid core nerve conduits were white in color, due to their porous structure, the surrounding blood moistened the conduits and turned them red. All experimental animals achieved primary wound healing after surgery, without skin redness and swelling and other

adverse reactions. MRI and 3D reconstruction of bilateral sciatic nerve regions of interest (ROI) were performed in the lower limbs of beagle dogs 1 year after surgery. The results showed that the sciatic nerve in Neurolac group was tortuous, the diameter of the nerve was uneven, and presented intermittent distribution. The reconstructed images of sheath and sheath & grid core groups presented a continuous distribution, showing bead-like changes. When the nerve sample was harvested, no exudation or abscess was observed in the soft tissue around the implantation site, and the specimens of each group were completely removed. Brightfield photographs of the harvested nerves showed that the grafts in the three groups were completely replaced by neural-like tissue, the material of all three groups had degraded without macroscopically visible scaffold remnants. However, in the Neurolac group, atrophy and collapse of the repaired area were observed, the repaired tissue was thin, the local continuity was interrupted, the color was dark, and a small amount of nerve appearance-like tissue was replaced. The sheath group also showed collapse of the repaired area and continuous passage of neuroid appearing tissue. In the sheath & grid core group, the regenerated nerve tissue was plump, vascular crawling growth was observed on the surface. The distal and proximal ends of the sciatic nerve were well integrated with the native nerve stump, and the morphology was the closest to that of the native nerve (Fig. 6C). We calculated the ratio of the diameter of the thinnest position of the regenerated nerve to the diameter of the native nerve in three groups and found that the ratio was significantly higher in the sheath & grid core group than in the other two groups (Supplementary Fig. 5).
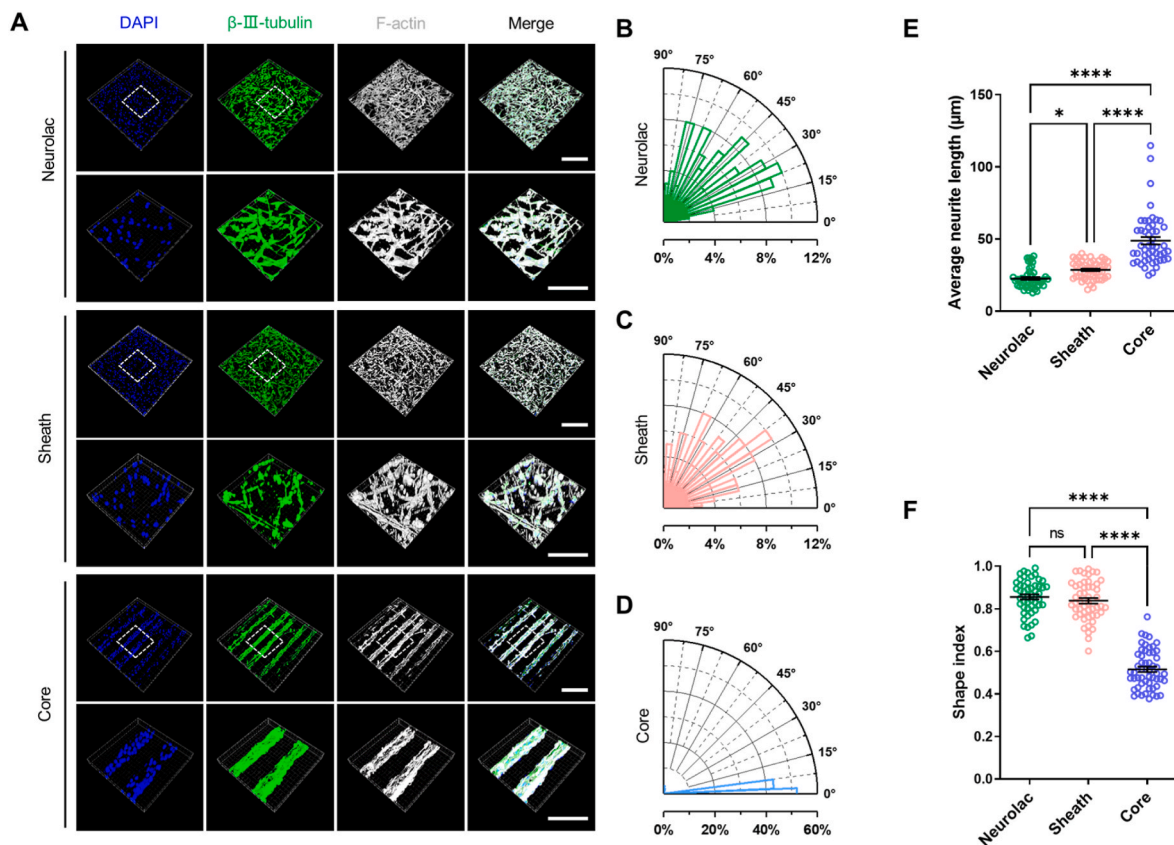
Fig. 4. PC12 cell behavior on different scaffolds. (A) Representative images of PC12 cells arranged and spread on the Neurolac scaffolds, sheath scaffolds, and grid core scaffolds, respectively. The second row of images in each group represent high-magnification images of the white box area. β-III-tubulin was stained in green, F-actin was stained grayish white, and cell nuclei was stained blue. **(B, C, D)** Nightingale rose plots of neurites orientation angle of the Neurolac scaffolds, sheath scaffolds, and grid core scaffolds, respectively. **(E)** The neurite length of Schwann cells on different scaffolds. **(F)** The shape index of PC12 cell nucleus. Scale bars: the first row of every group, 200 μm; the second row of every group, 100 μm. $n = 5$ for all groups.

3.7. Histology and histomorphometry of regenerated nerve

To further determine the promoting effect of core addition on nerve regeneration, we further performed histological analysis of the regenerated nerve 1 year after implantation, as shown in Fig. 7A, five segments of the regenerated nerve were analyzed. H&E staining revealed (Fig. 7B) that no residual fragments of the nerve conduit material were found in all three groups, indicating that the nerve conduit material had been completely degraded. Transverse sections showed that numerous inflammatory cells infiltrated into the epineurium of the middle segment of nerve in the Neurolac group. There were a few scattered nerve fiber bundles regeneration in the middle and distal segments of the regenerated nerve, and a large amount of connective tissue appeared between the nerve bundles in the Neurolac group. No obvious inflammatory cell infiltration was found in the Sheath group, and nerve fiber bundles regeneration in the middle segment were slightly better than that of the Neurolac group, but there was no significant histological difference in the nerve fiber of the distal segment between the Sheath group and the Neurolac Group. In Sheath & Core group, no obvious inflammatory cell infiltration was found. The nerve fibers in the middle segment regenerated into the primary nerve fascicles, which were evenly distributed, and thick nerve fiber bundles similar to native nerves appeared in the distal segment. Longitudinal sections showed that cells in Neurolac and Sheath groups presented irregular arrangement and were surrounded by loose and disordered ECM. The cells and ECM in Sheath & Core group, on the other hand, presented a dense and orderly parallel arrangement along the long axis. All the three groups showed good vascularization within the nerve bundle, between the nerve bundles and in the epineurium. We performed quantitative statistics on the number of

vessels in the middle and distal segments of the regenerated nerve, and the results showed that the number of vessels in the Sheath & Core group showed a tendency to be higher than that in the other two groups at both locations. In the middle segment, the number of vessels was significantly higher in the Sheath & Core group than in the Neurolac group (Fig. 7G), whereas in the distal segment, there was no significant difference in the number of vessels between the three groups (Fig. 7H). Masson trichrome staining showed that there was a large amount of collagen deposition in the epineurium of all three groups (Fig. 7C). Transverse sections showed limited numbers of myelinated nerve fibers and smaller nerve fiber diameters in both the Neurolac and Sheath groups, weather in the mid- or distal- segments. In Neurolac group, the distal nerve fascicles were partly degenerated, accompanied by proliferation of connective tissue, and blurring of perineurial boundaries. The density of myelinated nerve fibers in the Sheath & Core group was higher than that in the other two groups. Longitudinal sections showed that the nerve fibers in the Neurolac and sheath groups were homogeneously distributed, and the nerve fibers in the sheath & grid core group showed a continuous arrangement along the long axis, with myelin sheaths wrapping around the nerve fibers in a parallel and orderly manner. Toluidine Blue staining and Luxol Fast blue staining showed myelination in three groups (Fig. 7D and E). Transected sections showed lower myelin density and lower myelin thickness in the middle and distal segments of regenerated nerves in both Neurolac and Sheath groups. sheath & grid core group showed higher myelin density and greater myelin thickness in regenerated nerves. Longitudinal sections showed that myelin sheaths in the Neurolac and Sheath groups were thin and scattered and showed intermittent distribution, while myelin sheaths in the sheath & grid core group showed uniform and continuous parallel arrangement. TEM
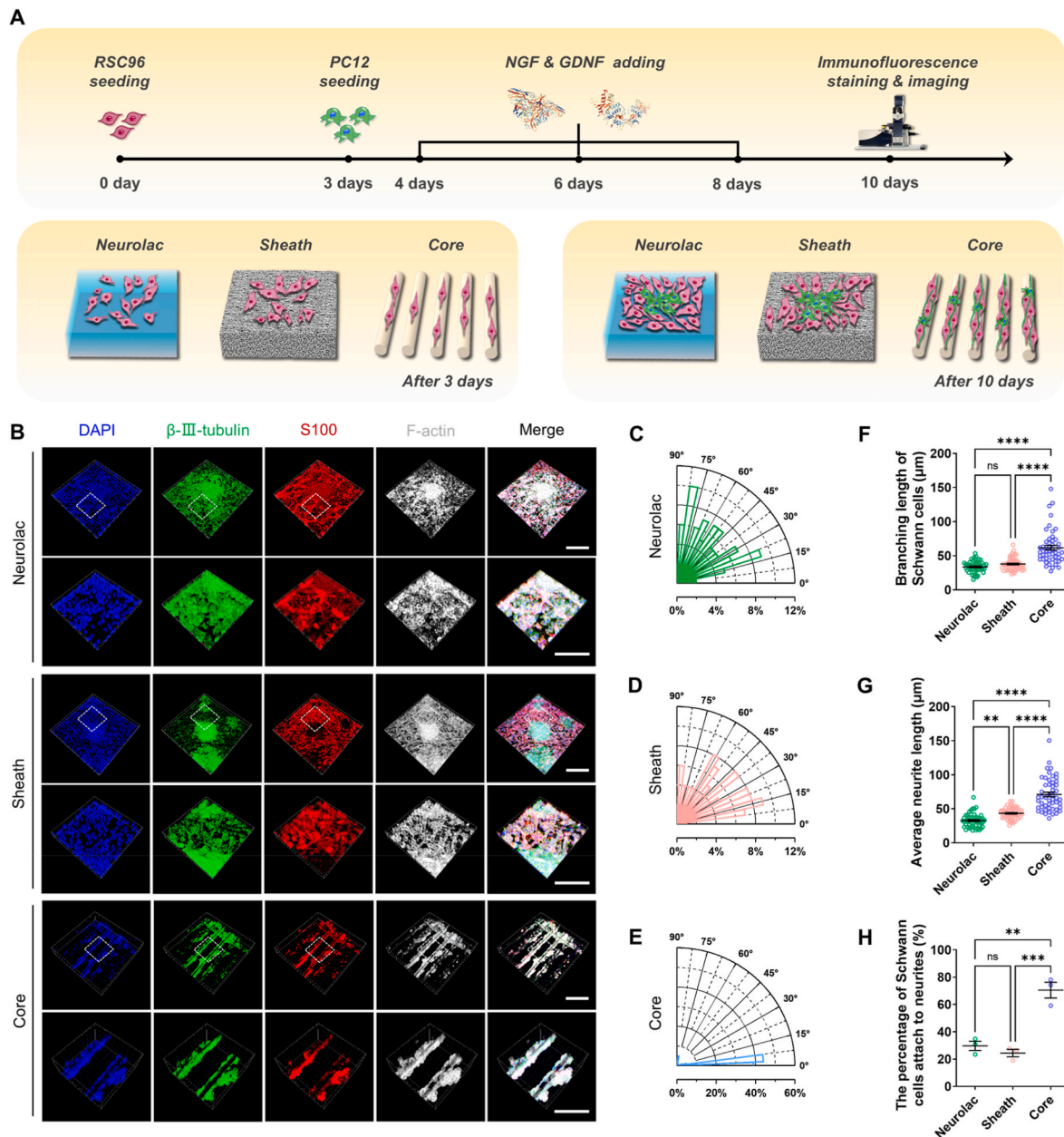
Fig. 5. Behavior of RSC96 cells co-cultured with PC12 cells on different scaffolds. (A) Schematic diagram of co-culture experiment protocol. **(B)** Representative pictures of the arrangement and co-localization of RSC96 cells with PC12 cells on the Neurolac scaffolds, sheath scaffolds, and grid core scaffolds. The second row of images in each group represent high-magnification images of the white box area. β-III-tubulin was stained in green, S100β was stained in red, F-actin was stained grayish white, and cell nuclei was stained blue. **(C, D, E)** Nightingale rose plots of Schwann cells and neurites arrangement angle of the Neurolac scaffolds, sheath scaffolds, and grid core scaffolds, respectively. **(F)** The branching length of Schwann cells on different scaffolds. **(G)** The neurite length of Schwann cells on different scaffolds. **(H)** The percentage of SCs attached along neurites over the total number of SCs. Scale bars: the first row of every group, 200 μm; the second row of every group, 100 μm. $n = 5$ for all groups.

images further showed the ultrastructure of the regenerated nerve (Fig. 7F). In the sheath & grid core graft group, the myelinated nerve fibers in the middle of the graft were densely clustered and dispersed, with a compact and homogeneous structure, and the number of unmyelinated fibers was significantly less than that in the other two groups. The density of myelinated nerve fibers in the distal end of sheath & grid core grafts was much higher than that in the other two groups, and the structure of perineurium was clearer. Further quantitative statistics of myelinated nerve fiber density showed that the density of myelinated nerve fibers was significantly higher in the sheath & grid core group than in the other two groups, both in the middle and distal segments of the regenerated nerve (Fig. 7I and J). The diameter of myelinated nerve

fibers in Sheath & Core group was also significantly higher than that in the other two groups in the middle and distal segments of the regenerated nerve. In the distal segment of the regenerated nerve, the diameter of axon was significantly larger in the Sheath group than in the Neurolac Group (Fig. 7K, L). Corresponding to the histological staining results, quantitative analysis of myelin thickness confirmed that in both the middle and distal segments of the regenerated nerve, myelin thickness was significantly higher in the sheath & grid core group than in the other two groups (Fig. 7M, N). The g-ratio of regenerating myelinated fibers, defined as the ratio of neurite inner diameter to outer diameter, was calculated to indicate the optimal function and structure of nerve myelination [28]. As shown in Fig. 7O and P, the g-ratio distribution
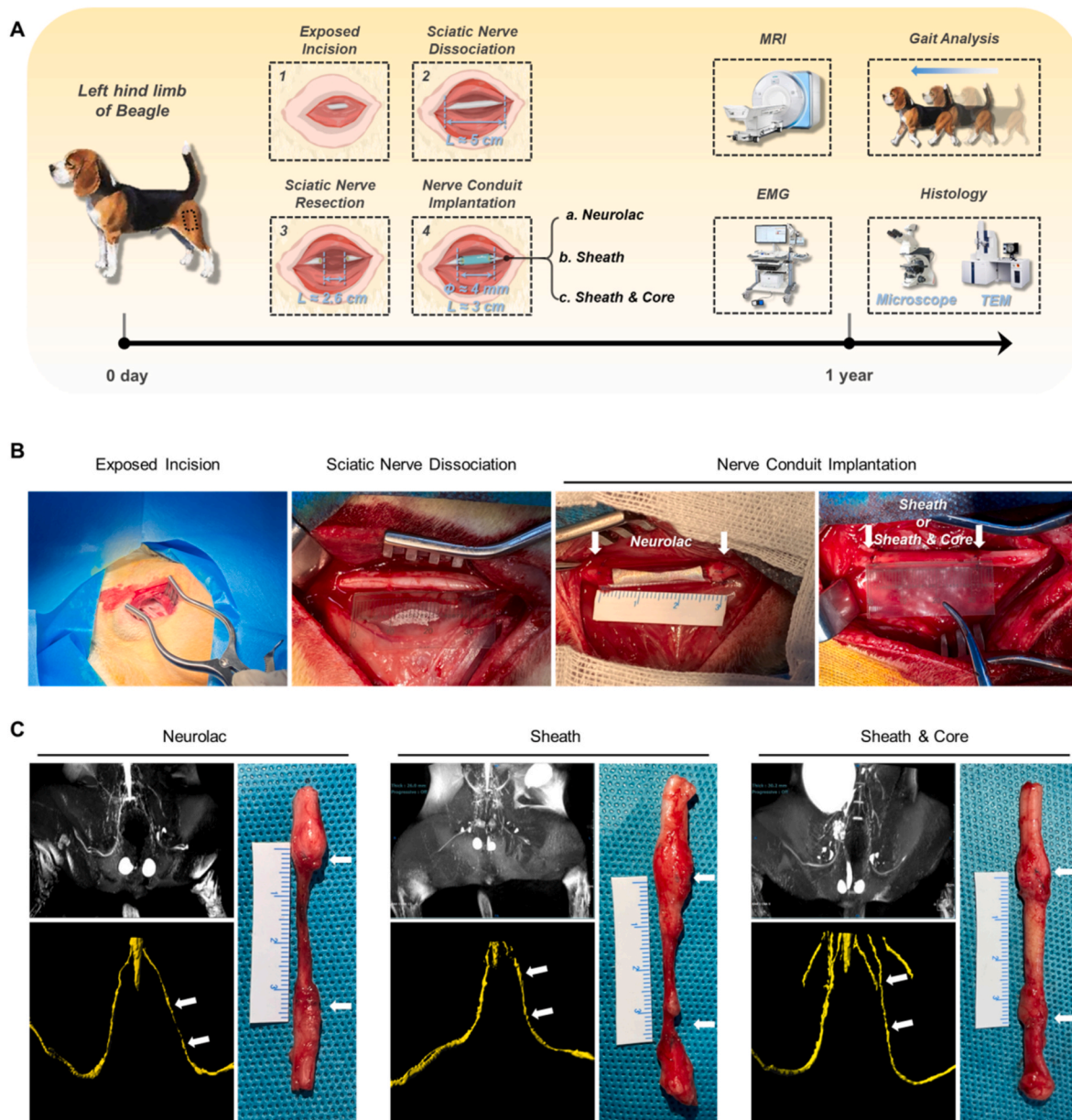
Fig. 6. In vivo implantation process of nerve conduit, MRI and 3D reconstruction images and gross morphology of regenerative nerve. (A) Schematic diagram of nerve conduit implantation process and corresponding detection. **(B)** Surgical procedure for nerve conduit implantation into the sciatic nerve of beagle dogs. **(C)** The MRI images (upper left), 3D reconstruction images (lower left), and gross pictures (right) of the Neurolac conduit, sheath conduit, sheath & grid core conduit 1 year after transplantation. $n = 3$ for all groups.

trend was very close between Neurolac group and Sheath group, while the g-ratio of sheath & grid core group was significantly smaller than that of the other two groups in both the middle and distal segments of the regenerated nerve (Supplementary Fig. 6 A, B).

3.8. Gait test and joint dynamic reconstruction

The recovery of motor ability of experimental animals directly reflects the level of regeneration of peripheral nerves. We performed a detailed assessment of the beagle dog's motor gait profile 1 year after surgery. All animals presented complete paralysis of their left hind legs immediately after sciatic nerve transection. With the regeneration of sciatic nerve after reconstruction, the motor status of operated limbs of experimental animals in each group showed differences. Photographs of the gait characteristics of each group of beagle dogs were shown in Fig. 8A. In the Neurolac group, the left hind leg of the dogs still

presented with severe paretic paralysis. During the gait cycle, dogs in the Neurolac group had limited active flexion of the left hock joints and metatarsophalangeal joints, the metatarsophalangeal joints presented mild hyperextension, plantar cannot be pressed flat and hind foot was prolapsed. In the Sheath group, the movement ability of the left hind leg was partially recovered, the active flexion movement of the hock joints and metatarsophalangeal joints showed partial recovery. The movement posture was still uncoordinated, and the sole of the hind foot could not be completely stepped flat. In the sheath & grid core group, the activity and muscle strength of each joint were significantly improved. During the gait cycle, it could be observed that the foot was able to tread flat, the pace of movement was regular, the movement posture was coordinated, and the posture was balanced.

At the same time, we dynamically reconstructed the changes of joint position of the hind leg during the gait cycle, which could more clearly and accurately show the motor recovery of experimental animals
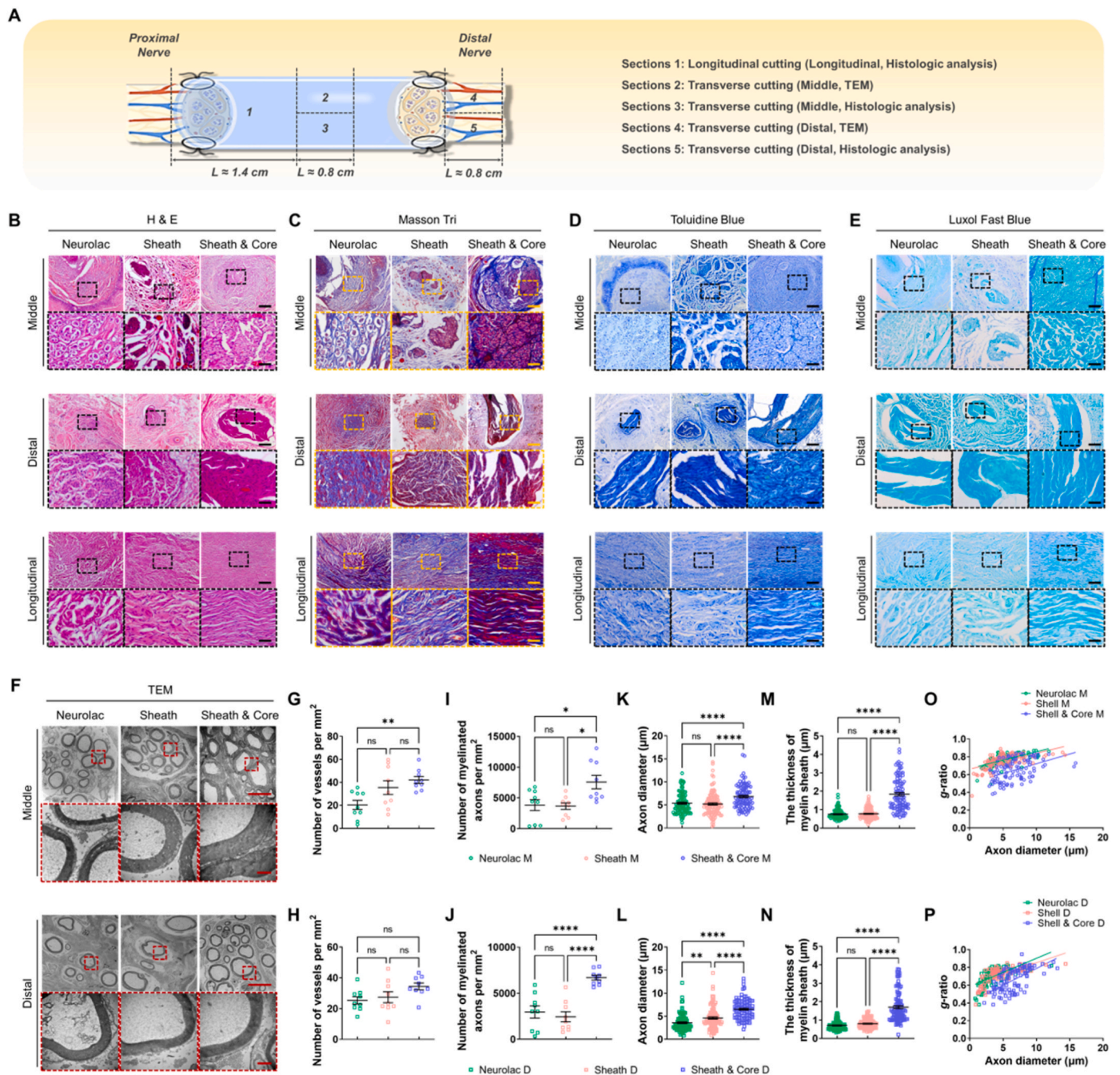
Fig. 7. Histological analysis of the nerve conduit 1 year after implantation. (A) Schematic diagram of analysis of regenerated nerve samples. **(B)** H&E staining of regenerated nerves. **(C)** Masson Trichrome staining of regenerated nerves. **(D)** Toluidine Blue staining of regenerated nerves. **(E)** Luxol Fast blue staining of regenerated nerves. **(F)** TEM pictures of regenerated nerves. **(G, H)** The vessel density in the middle and distal segments of the regenerated nerve. **(I, J)** The density of myelinated axons in the middle and distal segments of the regenerated nerve. **(K, L)** The diameter of axons in the middle and distal segments of the regenerated nerve. **(M, N)** The myelin thickness in the middle and distal segments of the regenerated nerve. **(O, P)** G-ratio distribution in relation to different axon diameters and the value of g-ratio of various groups. Scale bars: B, C, D, E, the first row of every segment, 200 μm; the second row of every segment, 50 μm. F, the first row of every segment, 10 μm; the second row of every segment, 1 μm. *n* = 3 for all groups.

(Fig. 8B, C, D). The flexion angles of the hock joints and metatarsophalangeal joints showed that the minimum active flexion angle of the hock (Fig. 8E) and metatarsophalangeal joints (Fig. 8F) were significantly smaller in the Sheath & Core group than in the Neurolac group, while there was no significant difference between the Sheath and Neurolac groups in these two angles. The motor function scores of the hind legs were shown in Fig. 8G, all animals received a gait score of 3 following nerve transection surgery. One year after surgery, one (1/3) Neurolac group improved to a score of 2, while the other two (2/3)

remained at a score of 3. In the Sheath group, one (1/3) improved to a score of 1, one (1/3) got a score of 2, and the remaining one (1/3) got a score of 3. In the sheath & grid core group, two (2/3) improved to a score of 1 and one (1/3) went up to a score of 2.

3.9. Histology and histomorphometry of regenerated nerve

To determine the functional recovery of sciatic nerve defects with different nerve conduits, we performed electrophysiological testing to
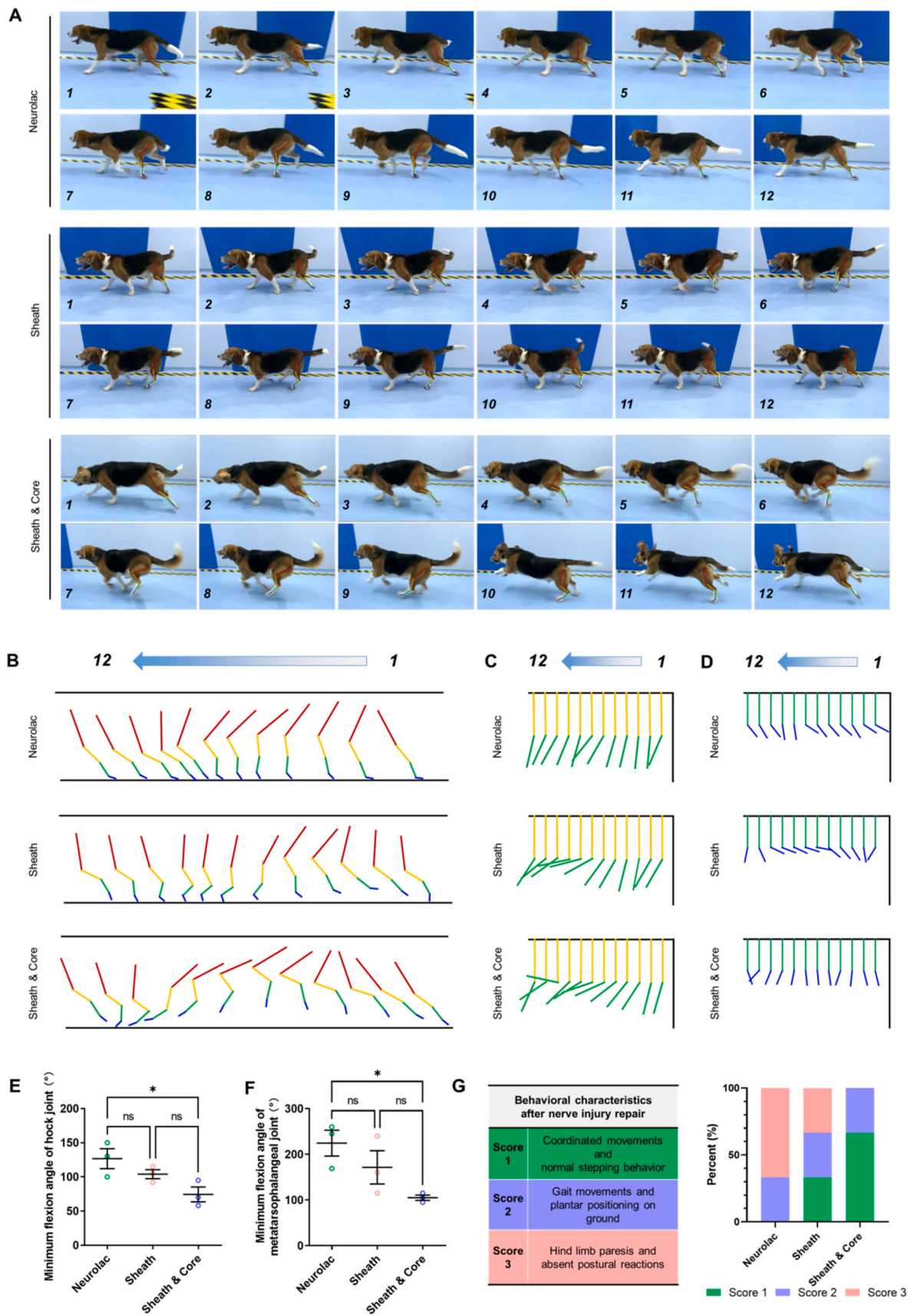
Fig. 8. Gait test, joint dynamic reconstruction, and motor function score. (A) Representative photographs of movement gait in each group of dogs 1 year after nerve conduit implantation. **(B)** Dynamic reconstructions of the left hind limb joints of dogs in each group. **(C)** Normalized dynamic reconstructions of the hock joints. **(D)** Normalized dynamic reconstructions of the metatarsophalangeal joints. **(E, F)** The minimum flexion angle of the hock and metatarsophalangeal joints in each group. **(G)** The motor function score of canines in each group. $n = 3$ for all groups.

assess the electrical transduction of regenerated nerves (Fig. 9A). The CMAP amplitude was significantly higher in the sheath & grid core group than in the other two groups (Fig. 9B). Meanwhile, the latency of nerve conduction was significantly shorter in the sheath & grid core group than in the other two groups (Fig. 9C). In MNCV, the sheath & grid core group was significantly faster than the Neurolac group, while there was no significant difference from the Sheath group (Fig. 9D). Atrophy of the gastrocnemius muscle, one of the target tissues of the sciatic nerve, was also evaluated to assess the function of the regenerated nerve. As observable in the 3D reconstruction images of MRI, the size of the gastrocnemius muscle on the experimental side (ES) was smaller than that on the normal side (NS), especially in the Neurolac group, where its muscle morphology was slender (Fig. 9E). The muscles of the ES in both sheath & grid core and sheath groups were red and lustrous in color, and quite soft in texture. However, the muscles of the ES in the Neurolac group were pale in color, hard and tenacious in texture with the severely atrophied muscle belly (Fig. 9F). The gastrocnemius muscle wet weight ratio (ES/NS) showed a decreasing trend from the sheath & grid core, sheath, and Neurolac groups, but there was no significant difference among the three groups (Fig. 9G). H&E staining of transverse sections showed that muscle fibers in the sheath & grid core group were uniform in size, muscle fibers in the sheath group had some degree of atrophy, and muscle fibers in the Neurolac group had severe atrophy, showing degradation and fragmentation of muscle fibers (Fig. 9H). Statistical data on muscle fiber diameter indicated that muscle fiber diameter was significantly larger in the sheath & grid core group than in the other two groups, while the sheath group also had a larger muscle fiber diameter than the Neurolac group (Fig. 9I). Masson's Trichrome staining confirmed extensive collagen deposition and muscle fibrosis around atrophic myofibers in Neurolac group, which were common features of muscle atrophy. In the other two groups, there were only a few collagen fibers between gastrocnemius muscle cells (Fig. 9J). The sheath & grid core Group, as well as the sheath group, had a statistically significantly smaller area of collagen fibers than the Neurolac group (Fig. 9K).

4. Discussion

The development of nerve conduits has shifted attention from the construction of simple hollow nerve conduits to the inclusion of biochemical factors (e.g., growth factors, active peptides, extracellular matrix, etc.) or biophysical cues (e.g., to guide Schwann cells, mesenchymal stem cells, etc.), with the aim to realize the improved repair of long-gap nerve defects [1,9]. However, these meaningful attempts to functionalize nerve conduits presents difficulty in terms of produced generalized conduits for the clinic and to address specific clinical needs within short timeframes [29]. Biophysical cues, due to their clarity of composition and structural plasticity, are expected to advance clinical applications of NGCs by introducing certain structural changes [22]. Because of the prospect of clinical translation, we chose FDA-approved polymers and used topological modulation to achieve long-distance nerve defect repair. Here, we constructed a composite nerve conduit composed of anisotropic microfiber grid cores and randomly organized nanofiber sheaths. The nanofiber sheaths possessed excellent elasticity, compression resistance and sufficient resistance to suture pull-out. The appropriate pore size prevented fibroblast infiltration while ensuring that transfer of nutrients and metabolic waste could proceed. The microfiber grid cores could direct Schwann cell and axon growth, by promoting axon elongation and increasing the adhesion ratio of Schwann cells to neurites. In beagle sciatic nerve defect models, our composite nerve conduits exhibited superior macroscopic morphology, neural integration, neurohistological regeneration, gait recovery, and
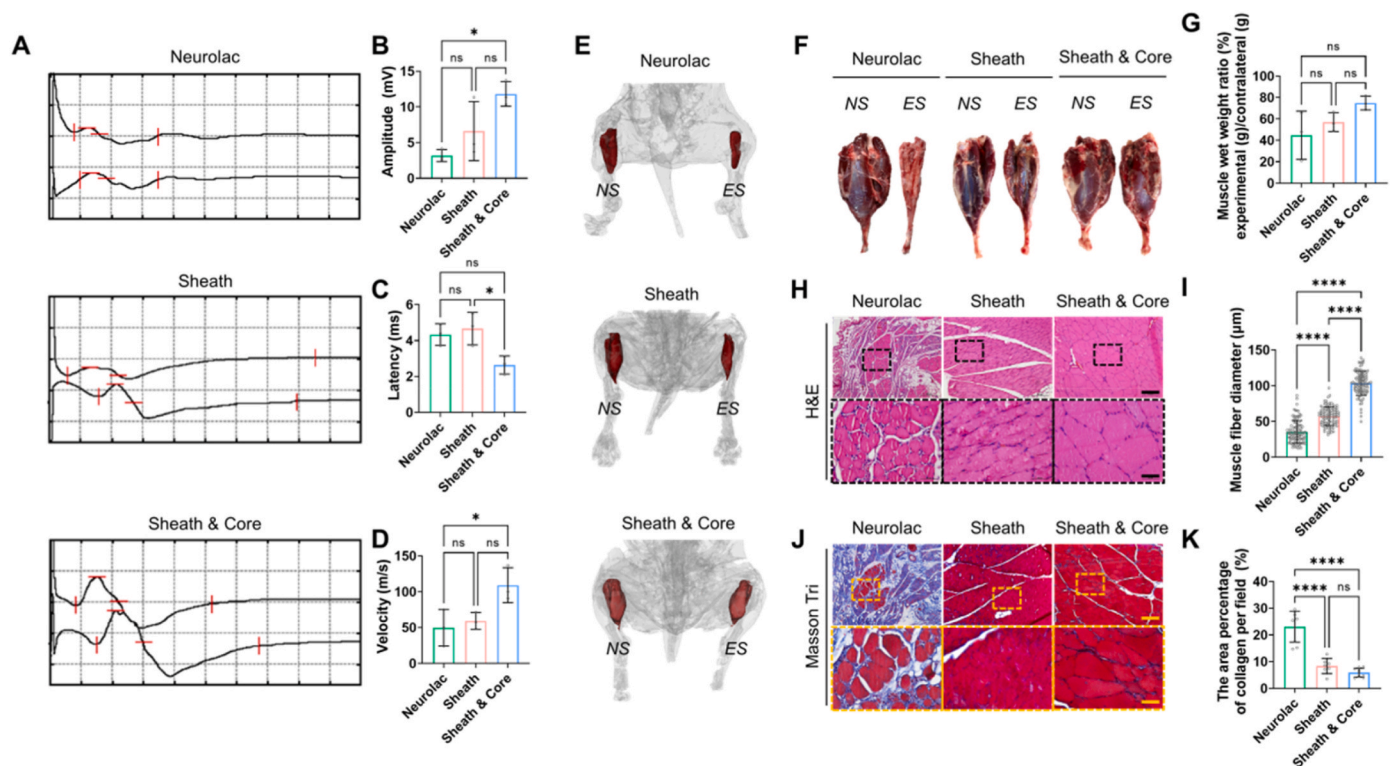

Fig. 9. Functional evaluation of regenerative nerve and gastrocnemius muscle atrophy 1 year after nerve conduit implantation. **(A)** Representative images of CMAP. **(B, C, D)** Quantitative analysis of CMAP amplitude, nerve conduction latency, and nerve conduction velocity. **(E, F)** Representative images of 3D reconstruction and gross view of gastrocnemius muscle on the experimental side (ES) and normal side (NS) of dogs. **(G)** Quantitative analysis of wet weight ratio of gastrocnemius muscle. **(H)** Representative microscopic images of H&E staining in cross sections of gastrocnemius muscle. **(I)** Quantitative analysis of muscle fiber diameter. **(J)** Representative microscopic images of Masson Tri staining of gastrocnemius muscle cross sections. **(K)** Quantitative analysis of area percentage of collagen. Scale bars: H, J, the first row, 200 μm; the second row, 50 μm. $n = 3$ for all groups.

electrophysiological and gastrocnemius muscle recovery compared with controls.

In currently published studies of nerve conduits, focus has tended to be on modification and innovation of internal fillers, but few studies have incorporated sheaths and assessed the benefit to nerve regeneration. Indeed, the mechanical properties of the sheaths were not only related to the convenience of clinical operation and suturing, but also affected nerve regeneration [16]. Under physiological conditions, nerves at joints undergo slight tension during joint movement. However, stretching also contributes to neuropathology, with some studies indicating that more than 5% nerve elongation could decrease conduction amplitude in an approximately linear manner [30,31]. Thus, if nerve conduits cannot support extension, they may adversely affect postoperative rehabilitation. At the same time, peripheral nerves tend to be with in a muscle-wrapped environment, exposing implanted nerve conduits to compression by surrounding tissues, which may result in reduced luminal volume and trigger of guidance failure [7,32]. To circumvent this, the use of polymers with elastic properties have been used to prepare sheathes for nerve conduits. PLCL is a hydrophobic aliphatic polyester copolymer obtained by ring-opening polymerization of PLA and PCL monomers. PLCL is highly elastic and has an adjustable degradation rate by changing molecular weight or the ratio of lactic acid to caprolactone. Moreover, PLCL has demonstrated its ability to maintain a stable shape during its biodegradation to its components polylactic acid and polycaprolactone in vivo, which are in-turn hydrolyzed to biocompatible lactic acid and 6-hydroxycaproic acid by-products [33,34]. In lieu of these advantages, PLCL has been approved for clinical use as nerve conduits, sutures, and controlled-release drug delivery systems by the FDA. The commercially available Neurolac nerve conduits are prepared from PLCL, thus making it an appropriate benchmark and control [35,36]. According to tensile test data of our nerve conduit Sheaths, the elongation at break was increased by 620%, and the lumen diameter was only reduced by 15% after 100 cycles of compression, which ensured that our composite conduits were unlikely to fail due to movement or compression by surrounding tissues. Appropriate strength for pull-out resistance should also be ensured to avoid risk of suture pull-out under traction of movement. Our nerve conduit sheaths demonstrated a pull-out resistance strength of 2.76 N, which was greater than the pull-out resistance strengths reported in the literature for Neurogen® products (1.80 N) [37].

Excessive fibroblast infiltration during nerve regeneration can result in the formation of scar tissue (i.e., neuroma formation) and hindered axonal regeneration [36]. The multilayer fibrous structure of our nerve conduit sheaths effectively limited the infiltration of fibroblasts, providing a barrier effect against fibroblasts, which didn't exhibit a significantly different outcome from that of Neurolac conduits that have a dense, nonporous structure. In addition, absorbable nerve conduits must be appropriately porous or permeable to allow for nutrients and waste products exchange between the cells within the conduit lumen and the exterior tissues, a process essential for initial revascularization and in ensuring the viability of supportive cells in the nerve regeneration process. Human growth factor proteins typically fall within the molecular weight range of several tens of kDa [38]. To test our sheaths' permeability, we used BSA, and its permeability served as an indicator that a supply of nutrients and growth factors could traverse the conduit sheaths during nerve regeneration. Moreover, good permeability also prevents pressure build-up caused by fluid retention, which has been suggested to lead to conduit collapse [39].

Achieving uniform orientation of guidance cues within the lumen of large-diameter nerve conduits is an important issue that required careful attention in this study. Commercially available nerve conduits such as Neurolac® and NeuraGen® are hollow, and both exhibit good reparative effects across short-gap nerve defects. However, the lack of appropriately scaled biophysical cues in these commercially available conduits has limited their capacity to repair long-gap (>3.0 cm) nerve defects [4,40]. To date, the most successful clinical substitutes for

autografts have been processed nerve allografts (Avance®, AxoGen). Following specialist decellularization treatment, these allograft products have preserved microarchitectural integrity that provides the necessary contact guidance for Schwann cell migration and axon elongation, thereby accelerating the process of nerve regeneration [11]. Consistent with this, increasing evidence has demonstrated that incorporation of intraluminal structures into hollow conduits serve as simple, yet effective, strategies to enhance contact guidance for nerve cells. Currently, guide fibers with a wide range of diameters (from 100 nm to 1000 μm) have been used to enhance contact guidance of nerve conduits and reduce axonal mismatch [41–47]. In our previous work, we showed that oriented guidance fibers close to the cell scale (approximately 20–30 μm) facilitated macrophage recruitment and subsequent polarization toward a pro-healing phenotype, which in-turn stimulated and promoted nerve regeneration [18]. Therefore, in this work, we followed a similar approach by using melt electroprinting to prepare anisotropic fibrous grid cores with fiber diameters of 22.64 ± 2.82 μm. The longitudinal fibers were densely arranged to guide directional adhesion and spreading of Schwann cells and axons, whereas transverse fibers were sparsely arranged to avoid misguidance to cells and to maintain the scaffold configuration. Compared with traditional guide fibers prepared by electrospinning [48–50], melt spinning [18], extrusion printing [2] or animal-tissue processing [20,21], melt electroprinting has an elevated printing accuracy, and the arrangement and diameter of fibers can be controlled with a high degree of precision [51,52]. More importantly, we found that grid cores printed by melt electroprinting remained uniformly spatially distributed when curled and filled into the lumen of large-diameter nerve conduits, removing the necessity for inclusion of stacked filling fibers, which is a commonly employed component in other nerve conduit fabrication procedures [1].

It was also important to match the degradation rate of the guiding fibers with the rate of nerve regeneration. If degradation rates are too fast, then an early loss of guidance effect may occur, whilst degradation rates that are too slow may trigger chronic inflammatory responses. Furthermore, the continuous space occupation by the material itself can affect the density of regenerated axons and may interfere with functional efficiency. Thus, biodegradable PDS was utilized as the grid core scaffolds for its moderate rate of degradation. PDS has been extensively investigated in tissue engineering studies, including its use as a polymer scaffold for biliary stents, biodegradable ring for pediatric mitral and tricuspid heart valve repair, etc [53]. PDS materials have been reported to completely degrade in vivo after 3–5 months, accompanied by low-order foreign body tissue reaction and absorption of its hydrolyzed by-products [54]. Combined with the nerve regeneration rate of 1–2 mm/day [7], the PDS degradation rate ensures axon guidance to the distal stump without nerve swelling due to prolonged non-degradation of scaffold polymers. In addition, PDS is flexible and possesses shape-memory properties, therein providing rebound and kink resistance [55], which further explains the observation of the PDS microfiber grid cores maintaining uniformity throughout the lumen.

In the present study, we demonstrated the successful repair of 3.0 cm canine sciatic nerve defects by using our developed nerve conduits. We achieved similar regenerative effects to other studies using beagle dogs as models without introducing additional seed cells and active substances [56,57]. We believe that by demonstrating the repair of nerve defects of critical length in large animal models can serve as a more robust NGC performance reference. The nerve conduit was completely degraded and was replaced by continuous tissue with nerve-like appearance that had successfully bridged the 30-mm sciatic nerve defect at 1-year post-implantation. Our composite nerve conduits showed significantly enhanced vascularization of the regenerated nerve tissue, with greater myelin density, myelin thickness, and axonal diameter compared to sheath-only conduits or commercially available Neurolac. Furthermore, our nerve conduits achieved the formation of dense, orderly, and parallelly arranged nerve cells and ECM along the whole length of the neotissue. An important aspect that measures the

extent of nerve repair is the g-ratio, which is closely related to the conduction velocity of myelinated nerve fibers. The g- ratio in the composite nerve conduit group matched the reported autograft values (approximately 0.65) [17], showing middle (0.65 ± 0.12) and distal (0.66 ± 0.13) segment g-ratios. The histological data suggested that our electroprinted grid core structures provided sufficient directional guidance for axon growth whilst also facilitating the promotion of axonal maturation.

Currently, studies that assess functional nerve recovery in murine models have utilized classical walking trajectory analysis to assess sciatic nerve motor function. Such an analysis method is limited in its reflection of the 3D spatial limb-joint movements made by larger animal models. Quantitative analysis methods suitable for assessing large animal models remain to be fully standardized [6,7,17]. Therefore, we made the decision to record canine movement gait using high-speed cameras to precisely quantify the movement gait. We performed frame-by-frame analysis of movement trajectory, and the joints of the left hind limb were dynamically reconstructed into data for visualization. Here, we refer to the research work of Lai et al. [58] and Jaegger et al. [59], wherein normalized reconstruction of the hock and metatarsophalangeal joints, the minimum flexion angle of the two joints were quantified, and the movement status of the animals could be further evaluated. Our results showed that the motor function of the left hind limb could be restored by our composite nerve conduit, which served as direct evidence that the regenerated nerve had successfully bridged the defect area to facilitate the regain of muscle control.

The amplitude of CMAP is directly proportional to the number of nerve fibers innervating the muscle and allows for the calculation of the conduction velocity of motor nerves [17]. Thus, CMAP examination provides an important index for the conductive function of peripheral nerves. Here, our composite nerve conduits showed enhanced recovery in both CMAP amplitude and conduction velocity. Denervation of target muscles occurs in motor nerve injuries, and is followed by alterations in various biological aspects, including gene expression, cellular ultrastructure, and neuromuscular junction mechanisms. These changes induce a shift in protein metabolism, transitioning from protein synthesis to protein degradation, which results in reduced muscle fiber volume, eventual muscle atrophy, and hyperplasia of connective tissues [60,61]. If muscles are reinnervated, function is recovered, and atrophy ceases. In this study, the gastrocnemius muscle was taken as a representative of the target muscle of the sciatic nerve, and there were no statistically significant differences in gastrocnemius muscle wet weight amongst the three implantation groups after 1 year of implantation. However, our composite nerve conduits demonstrated qualitatively improved gastrocnemius muscle morphology, muscle fiber diameter, and an absence of muscle fibrosis. These findings were consistent with the electrophysiological assessments and collectively provided evidence that the grid core structures promoted functional regeneration of the sciatic nerve and achieved target muscle reinnervation.

We have demonstrated the applicability of our engineered composite nerve conduits with specialized polymeric structures in nerve regeneration. Our conduits exhibited appropriate mechanical properties, permeability, acted as barriers against fibroblast infiltration, and facilitated effective neural cell guidance. Repair of canine sciatic nerve injuries up to 3.0 cm in length was achieved in vivo, and comprehensive recovery at the neuromorphological, histological, and functional levels was observed. Limited by the size of the control product Neurolac® (maximum length of 3.0 cm), we limited testing in this study to nerve defect models of 3.0 cm in length. In future work, a reasonable direction would be to assess the efficacy of our composite nerve conduits for the repair of larger defects. In addition, different from the research performed in murine models, post-operation nursing and exercise rehabilitation carry more importance in the process of nerve regeneration in large animal models, which represents an area of the research field that requires interdisciplinary insight for further exploration.

5. Conclusion

In summary, this study demonstrated the feasibility of acellular, synthetic, composite nerve conduits to promote nerve regeneration in vivo. Our engineered conduits demonstrated the options offered by fabrication technologies and new possibilities for identifying alternatives to allograft and autograft repair of nerve defects. We provided an experimental basis that establishes the rationale for the implication of synthetic nerve conduits for implant to bridge long-gap nerve defects and for promoting the formation of tissue engineered nerve neotissue. Furthermore, our composite nerve conduits do not require chemical or biological modifications and demonstrate reproducibility and stability in their manufacture. The ease of storage and disinfection of our conduits indicate their use as readily available 'off-the-shelf' products that are expected to advance application in subsequent studies on their potential for clinical transformation.

Ethics approval and consent to participate

All animal studies were performed according to the guidelines set by the Tianjin Committee of Use and Care of Laboratory Animals, and the overall project protocols were approved by the Animal Ethics Committee of Nankai University. The accreditation number of the laboratory is SYXK (Jin) 2019–0003 promulgated by the Tianjin Science and Technology Commission.

CRediT authorship contribution statement

Xianhao Dong: Conceptualization, Data curation, Formal analysis, Investigation, Methodology, Visualization, Writing – original draft, Writing – review & editing, Funding acquisition. **Yueyue Yang:** Data curation, Formal analysis, Investigation, Visualization. **Zheheng Bao:** Methodology, Data curation, Formal analysis, Validation, Writing – review & editing. **Adam C. Midgley:** Writing – original draft, Writing – review & editing. **Feiyi Li:** Formal analysis, Validation. **Shuxin Dai:** Formal analysis, Validation. **Zhuangzhuang Yang:** Formal analysis, Validation. **Jin Wang:** Resources, Methodology. **Lihua Liu:** Resources, Methodology. **Wenlei Li:** Formal analysis, Validation. **Yayuan Zheng:** Formal analysis, Validation. **Siyang Liu:** Formal analysis. **Yang Liu:** Resources, Software. **Weijian Yu:** Validation. **Jun Liu:** Investigation. **Meng Fan:** Supervision, Project administration, Resources, Methodology, Writing – original draft, Writing – review & editing, Funding acquisition. **Meifeng Zhu:** Conceptualization, Supervision, Project administration, Resources, Writing – original draft, Writing – review & editing, Funding acquisition. **Zhongyang Shen:** Writing – review & editing. **Gu Xiaosong:** Writing – review & editing. **Deling Kong:** Supervision, Project administration, Resources, Writing – original draft, Writing – review & editing, Funding acquisition.

Declaration of competing interest

The authors declare no conflict of interest.

Acknowledgements

Appendix A. Supplementary data

Supplementary data to this article can be found online at https://doi.

org/10.1016/j.bioactmat.2023.06.015.

References

[1] A. Faroni, S.A. Mobasseri, P.J. Kingham, A.J. Reid, Peripheral nerve regeneration: experimental strategies and future perspectives, Adv. Drug Deliv. Rev. 82–83 (2015) 160–167.

[2] K. Liu, L. Yan, R. Li, Z. Song, J. Ding, B. Liu, X. Chen, 3D printed personalized nerve guide conduits for precision repair of peripheral nerve defects, Adv. Sci. 9 (2022), e2103875.

[3] C. Lubetzki, B. Zalc, A. Williams, C. Stadelmann, B. Stankoff, Remyelination in multiple sclerosis: from basic science to clinical translation, Lancet Neurol. 19 (2020) 678–688.

[4] C.E. Schmidt, J.B. Leach, Neural tissue engineering: strategies for repair and regeneration, Annu. Rev. Biomed. Eng. 5 (2003) 293–347.

[5] L. Li, R. Hao, J. Qin, J. Song, X. Chen, F. Rao, J. Zhai, Y. Zhao, L. Zhang, J. XueElectrospun fibers control drug delivery for tissue regeneration and cancer therapy, Adv. Fiber Mater. 4 (2022) 1375–1413.

[6] N.B. Fadia, J.M. Bliley, G.A. DiBernardo, D.J. Crammond, B.K. Schilling, W. N. Sivak, A.M. Spiess, K.M. Washington, M. Waldner, H.T. Liao, I.B. James, D. M. Minteer, C. Tompkins-Rhoades, A.R. Cottrill, D.Y. Kim, R. Schweizer, D. A. Bourne, G.E. Panagis, M. Asher Schusterman 2nd, F.M. Egro, I.K. Campwala, T. Simpson, D.J. Weber, T. Gause 2nd, J.E. Brooker, T. Josyula, A.A. Guevara, A. J. Repko, C.M. Mahoney, K.G. Marra, Long-gap peripheral nerve repair through sustained release of a neurotrophic factor in nonhuman primates, Sci. Transl. Med. 12 (527) (2020), eaav7753.

[7] D.H. Smith, J.C. Burrell, K.D. Browne, K.S. Katiyar, M.I. Ezra, J.L. Dutton, J. P. Morand, L.A. Struzyna, F.A. Laimo, H.I. Chen, J.A. Wolf, H.M. Kaplan, J. M. Rosen, H.C. Ledebur, E.L. Zager, Z.S. Ali, D.K. Cullen, Tissue-engineered grafts exploit axon-facilitated axon regeneration and pathway protection to enable recovery after 5-cm nerve defects in pigs, Sci. Adv. 8 (2022), eabm3291.

[8] B. Gong, X. Zhang, A.A. Zahrani, W. Gao, G. Ma, L. Zhang, J. Xue, Explorations 2 (2022), 20210035.

[9] A.R. Dixon, S.H. Jariwala, Z. Bilis, J.R. Loverde, P.F. Pasquina, L.M. Alvarez, Bridging the gap in peripheral nerve repair with 3D printed and bioprinted conduits, Biomaterials 186 (2018) 44–63.

[10] X. Gu, F. Ding, D.F. Williams, Neural tissue engineering options for peripheral nerve regeneration, Biomaterials 35 (2014) 6143–6156.

[11] M. Kasper, C. Deister, F. Beck, C.E. Schmidt, Bench-to-Bedside lessons learned: commercialization of an acellular nerve graft, Adv Healthc Mater 9 (2020), e2000174.

[12] R. Schmidhammer, S. Zandieh, R. Hopf, I. Mizner, L.E. Pelinka, A. Kroepfl, H. Redl, Alleviated tension at the repair site enhances functional regeneration: the effect of full range of motion mobilization on the regeneration of peripheral nerves–histologic, electrophysiologic, and functional results in a rat model, J. Trauma 56 (2004) 571–584.

[13] P.J. Johnson, P. Newton, D.A. Hunter, S.E. Mackinnon, Nerve endoneurial microstructure facilitates uniform distribution of regenerative fibers: a post hoc comparison of midgraft nerve fiber densities, J. Reconstr. Microsurg. 27 (2011) 83–90.

[14] I. Ducic, R. Fu, M.L. Iorio, Innovative treatment of peripheral nerve injuries: combined reconstructive concepts, Ann. Plast. Surg. 68 (2012) 180–187.

[15] B. Safa, J.T. Shores, J.V. Ingari, R.V. Weber, M. Cho, J. Zoldos, T.R. Niacaras, L. J. Nesti, W.P. Thayer, G.M. Buncke, Recovery of motor function after mixed and motor nerve repair with processed nerve allograft, Plast Reconstr. Surg. Glob. Open 7 (2019) e2163.

[16] Q. Quan, H. Meng, B. Chang, L. Hong, R. Li, G. Liu, X. Cheng, H. Tang, P. Liu, Y. Sun, J. Peng, Q. Zhao, Y. Wang, S. Lu, Novel 3-D helix-flexible nerve guide conduits repair nerve defects, Biomaterials 207 (2019) 49–60.

[17] X. Wang, W. Hu, Y. Cao, J. Yao, J. Wu, X. Gu, Dog sciatic nerve regeneration across a 30-mm defect bridged by a chitosan/PGA artificial nerve graft, Brain 128 (2005) 1897–1910.

[18] X. Dong, S. Liu, Y. Yang, S. Gao, W. Li, J. Cao, Y. Wan, Z. Huang, G. Fan, Q. Chen, H. Wang, M. Zhu, D. Kong, Aligned microfiber-induced macrophage polarization to guide schwann-cell-enabled peripheral nerve regeneration, Biomaterials 272 (2021) 120767.

[19] N. Hu, H. Wu, C. Xue, Y. Gong, J. Wu, Z. Xiao, Y. Yang, F. Ding, X. Gu, Long-term outcome of the repair of 50 mm long median nerve defects in rhesus monkeys with marrow mesenchymal stem cells-containing, chitosan-based tissue engineered nerve grafts, Biomaterials 34 (2013) 100–111.

[20] Y. Cui, C. Lu, D. Meng, Z. Xiao, X. Hou, W. Ding, D. Kou, Y. Yao, B. Chen, Z. Zhang, J. Li, J. Pan, J. Dai, Collagen scaffolds modified with CNTF and bFGF promote facial nerve regeneration in minipigs, Biomaterials 35 (2014) 7819–7827.

[21] T. Kornfeld, J. Nessler, C. Helmer, R. Hannemann, K.H. Waldmann, C.T. Peck, P. Hoffmann, G. Brandes, P.M. Vogt, C. Radtke, Spider silk nerve graft promotes axonal regeneration on long distance nerve defect in a sheep model, Biomaterials 271 (2021), 120692.

[22] Y. Li, S. Lv, H. Yuan, G. Ye, W. Mu, Y. Fu, X. Zhang, Z. Feng, Y. He, W. Chen, Peripheral nerve regeneration with 3D printed bionic scaffolds loading neural crest stem cell derived schwann cell progenitors, Adv. Funct. Mater. 31 (2021), 2010215.

[23] A.J. Vernadakis, H. Koch, S.E. Mackinnon, Management of neuromas, Clin. Plast. Surg. 30 (2003) 247–268 (vii).

[24] T. Kornfeld, P.M. Vogt, V. Bucan, C.T. Peck, K. Reimers, C. Radtke, Characterization and schwann cell seeding of up to 15.0 cm long spider silk nerve

[25] M. Haim Zada, A. Kumar, O. Elmalak, G. Mechrez, A.J. Domb, Effect of ethylene oxide and gamma (gamma-) sterilization on the properties of a PLCL polymer material in balloon implants, ACS Omega 4 (2019) 21319–21326.

[26] A. Malheiro, F. Morgan, M. Baker, L. Moroni, P. Wieringa, A three-dimensional biomimetic peripheral nerve model for drug testing and disease modelling, Biomaterials 257 (2020), 120230.

[27] J.L. Zou, S. Liu, J.H. Sun, W.H. Yang, Y.W. Xu, Z.L. Rao, B. Jiang, Q.T. Zhu, X. L. Liu, J.L. Wu, Peripheral nerve-derived matrix hydrogel promotes remyelination and inhibits synapse formation, Adv. Funct. Mater. 28 (2018), 1705739.

[28] T. Chomiak, B. Hu, What is the optimal value of the g-ratio for myelinated fibers in the rat CNS? A theoretical approach, PLoS One 4 (2009), e7754.

[29] T. Kornfeld, P.M. Vogt, C. Radtke, Nerve grafting for peripheral nerve injuries with extended defect sizes, Wien Med. Wochenschr. 169 (2019) 240–251.

[30] N. Manvell, J.J. Manvell, S.J. Snodgrass, S.A. Reid, Tension of the ulnar, median, and radial nerves during ulnar nerve neurodynamic testing: observational cadaveric study, Phys. Ther. 95 (2015) 891–900.

[31] J.J. Manvell, N. Manvell, S.J. Snodgrass, S.A. Reid, Improving the radial nerve neurodynamic test: an observation of tension of the radial, median and ulnar nerves during upper limb positioning, Man. Ther. 20 (2015) 790–796.

[32] M. Stossel, V.M. Wildhagen, O. Helmecke, J. Metzen, C.B. Pfund, T. Freier, K. Haastert-Talini, Comparative evaluation of chitosan nerve guides with regular or increased bendability for acute and delayed peripheral nerve repair: a comprehensive comparison with autologous nerve grafts and muscle-in-vein grafts, Anat. Rec. 301 (2018) 1697–1713.

[33] V. Wong, The science of absorbable poly(L-lactide-Co-epsilon-Caprolactone) threads for soft tissue repositioning of the face: an evidence-based evaluation of their physical properties and clinical application, Clin. Cosmet. Invest. Dermatol. 14 (2021) 45–54.

[34] J. Fernandez, A. Etxeberria, J.R. Sarasua, Synthesis, structure and properties of poly(L-lactide-co-epsilon-caprolactone) statistical copolymers, J. Mech. Behav. Biomed. Mater. 9 (2012) 100–112.

[35] S. Kehoe, X.F. Zhang, D. Boyd, FDA approved guidance conduits and wraps for peripheral nerve injury: a review of materials and efficacy, Injury 43 (2012) 553–572.

[36] W.F. den Dunnen, M.F. Meek, Sensory nerve function and auto-mutilation after reconstruction of various gap lengths with nerve guides and autologous nerve grafts, Biomaterials 22 (2001) 1171–1176.

[37] S. Madduri, K. Feldman, T. Tervoort, M. Papaloizos, B. Gander, Collagen nerve conduits releasing the neurotrophic factors GDNF and NGF, J. Contr. Release 143 (2010) 168–174.

[38] J. Lee, E.H. Jang, J.H. Kim, S. Park, Y. Kang, S. Park, K. Lee, J.H. Kim, Y.N. Youn, W. Ryu, Highly flexible and porous silk fibroin microneedle wraps for perivascular drug delivery, J. Contr. Release 340 (2021) 125–135.

[39] E. Schnell, K. Klinkhammer, S. Balzer, G. Brook, D. Klee, P. Dalton, J. Mey, Guidance of glial cell migration and axonal growth on electrospun nanofibers of poly-epsilon-caprolactone and a collagen/poly-epsilon-caprolactone blend, Biomaterials 28 (2007) 3012–3025.

[40] L.B. Dahlin, Techniques of peripheral nerve repair, Scand. J. Surg. 97 (2008) 310–316.

[41] D. Hoffman-Kim, J.A. Mitchel, R.V. Bellamkonda, Topography, cell response, and nerve regeneration, Annu. Rev. Biomed. Eng. 12 (2010) 203–231.

[42] J. Cao, C. Sun, H. Zhao, Z. Xiao, B. Chen, J. Gao, T. Zheng, W. Wu, S. Wu, J. Wang, J. Dai, The use of laminin modified linear ordered collagen scaffolds loaded with laminin-binding ciliary neurotrophic factor for sciatic nerve regeneration in rats, Biomaterials 32 (2011) 3939–3948.

[43] S.Y. Chew, R. Mi, A. Hoke, K.W. Leong, Aligned protein-polymer composite fibers enhance nerve regeneration: a potential tissue-engineering platform, Adv. Funct. Mater. 17 (2007) 1288–1296.

[44] L. Zhan, J. Deng, Q. Ke, X. Li, Y.M. Ouyang, C. Huang, X.Q. Liu, Y. Qian, Grooved fibers: preparation principles through electrospinning and potential applications, Adv. Fiber Mater. 4 (2) (2022) 203–213.

[45] S. Wang, Q.C. Xu, H. Sun, Functionalization of fiber devices: materials, preparations and applications, Adv. Fiber Mater. 4 (3) (2022) 324–341.

[46] G. Li, T. Zheng, L. Wu, Q. Han, Y. Lei, L. Xue, L. Zhang, X. Gu, Y. Yang, Bionic microenvironment-inspired synergistic effect of anisotropic micro-nanocomposite topology and biology cues on peripheral nerve regeneration, Sci. Adv. 7 (28) (2021) eabi5812.

[47] X. Yao, L. Zhan, Z. Yan, J. Li, L. Kong, X. Wang, H. Xiao, H. Jiang, C. Huang, Y. Ouyang, Y. Qian, C. Fan, Non-electric bioelectrical analog strategy by a biophysical-driven nano-micro spatial anisotropic scaffold for regulating stem cell niche and tissue regeneration in a neuronal therapy, Bioact. Mater. 20 (2022) 319–338.

[48] B.K. Lee, Y.M. Ju, J.G. Cho, J.D. Jackson, S.J. Lee, A. Atala, J.J. Yoo, End-to-side neurorrhaphy using an electrospun PCL/collagen nerve conduit for complex peripheral motor nerve regeneration, Biomaterials 33 (2012) 9027–9036.

[49] L. Zhu, K. Wang, T. Ma, L. Huang, B. Xia, S. Zhu, Y. Yang, Z. Liu, X. Quan, K. Luo, D. Kong, J. Huang, Z. Luo, Noncovalent bonding of RGD and YIGSR to an electrospun poly(epsilon-caprolactone) conduit through peptide self-assembly to synergistically promote sciatic nerve regeneration in rats, Adv. Healthc Mater 6 (2017), 1600860.

[50] B. Jin, Y. Yu, C. Lou, X. Zhang, B. Gong, J. Chen, X. Chen, Z. Zhou, L. Zhang, J. Xiao, J. Xue, Combining a density gradient of biomacromolecular nanoparticles with biological effectors in an electrospun fiber-based nerve guidance conduit to promote peripheral nerve repair, Adv. Sci. 10 (4) (2023), e2203296.

[51] Z. Zhang, M.L. Jorgensen, Z. Wang, J. Amagat, Y. Wang, Q. Li, M. Dong, M. Chen, 3D anisotropic photocatalytic architectures as bioactive nerve guidance conduits for peripheral neural regeneration, Biomaterials 253 (2020), 120108.

[52] J. Wang, H. Wang, X. Mo, H. Wang, Reduced graphene oxide-encapsulated microfiber patterns enable controllable formation of neuronal-like networks, Adv. Mater. 32 (2020), e2004555.

[53] N. Goonoo, R. Jeetah, A. Bhaw-Luximon, D. Jhurry, Polydioxanone-based biomaterials for tissue engineering and drug/gene delivery applications, Eur. J. Pharm. Biopharm. 97 (2015) 371–391.

[54] J.A. Ray, N. Doddi, D. Regula, J.A. Williams, A. Melveger, Polydioxanone (PDS), a novel monofilament synthetic absorbable suture, Surg. Gynecol. Obstet. 153 (1981) 497–507.

[55] E.D. Boland, B.D. Coleman, C.P. Barnes, D.G. Simpson, G.E. Wnek, G.L. Bowlin, Electrospinning polydioxanone for biomedical applications, Acta Biomater. 1 (2005) 115–123.

[56] Y. Kaizawa, R. Kakinoki, R. Ikeguchi, S. Ohta, T. Noguchi, H. Oda, S. Matsuda, Bridging a 30 mm defect in the canine ulnar nerve using vessel-containing conduits with implantation of bone marrow stromal cells, Microsurgery 36 (2016) 316–324.

[57] M.H. Daradka, Z.A. Bani Ismail, M.A. Irsheid, Peripheral nerve regeneration: a comparative study of the effects of autologous bone marrow-derived mesenchymal stem cells, platelet-rich plasma, and lateral saphenous vein graft as a conduit in a dog model, Open Vet. J. 11 (2021) 686–694.

[58] B.Q. Lai, M.T. Che, B. Feng, Y.R. Bai, G. Li, Y.H. Ma, L.J. Wang, M.Y. Huang, Y. Q. Wang, B. Jiang, Y. Ding, X. Zeng, Y.S. Zeng, Tissue-engineered neural network graft relays excitatory signal in the completely transected canine spinal cord, Adv. Sci. 6 (2019), 1901240.

[59] G. Jaegger, D.J. Marcellin-Little, D. Levine, Reliability of goniometry in labrador retrievers, Am. J. Vet. Res. 63 (2002) 979–986.

[60] S.C. Bodine, E. Latres, S. Baumhueter, V.K. Lai, L. Nunez, B.A. Clarke, W. T. Poueymirou, F.J. Panaro, E. Na, K. Dharmarajan, Z.Q. Pan, D.M. Valenzuela, T. M. DeChiara, T.N. Stitt, G.D. Yancopoulos, D.J. Glass, Identification of ubiquitin ligases required for skeletal muscle atrophy, Science 294 (2001) 1704–1708.

[61] J. Ijkema-Paassen, M.F. Meek, A. Gramsbergen, Transection of the sciatic nerve and reinnervation in adult rats: muscle and endplate morphology, Equine Vet J Suppl 33 (2001) 41–45.